EXPERIMENTAL METHOD OF GENERATING ELECTROMAGNETIC GAUSSIAN SCHELL-MODEL BEAMS

THESIS

Matthew J. Gridley, Captain, USAF

AFIT-ENG-MS-15-M-058

DEPARTMENT OF THE AIR FORCE
AIR UNIVERSITY

AIR FORCE INSTITUTE OF TECHNOLOGY

Wright-Patterson Air Force Base, Ohio

DISTRIBUTION STATEMENT A:
APPROVED FOR PUBLIC RELEASE; DISTRIBUTION UNLIMITED

The views expressed in this thesis are those of the author and do not reflect the official policy or position of the United States Air Force, the Department of Defense, or the United States Government.

This material is declared a work of the U.S. Government and is not subject to copyright protection in the United States.

AFIT-ENG-MS-15-M-058

EXPERIMENTAL METHOD OF GENERATING ELECTROMAGNETIC GAUSSIAN SCHELL-MODEL BEAMS

THESIS

Presented to the Faculty

Department of Electrical and Computer Engineering

Graduate School of Engineering and Management

Air Force Institute of Technology

Air University

Air Education and Training Command

in Partial Fulfillment of the Requirements for the

Degree of Master of Science in Electrical Engineering

Matthew J. Gridley, B.S.E.E.

Captain, USAF

March 2015

DISTRIBUTION STATEMENT A:
APPROVED FOR PUBLIC RELEASE; DISTRIBUTION UNLIMITED

AFIT-ENG-MS-15-M-058

EXPERIMENTAL METHOD OF GENERATING ELECTROMAGNETIC GAUSSIAN SCHELL-MODEL BEAMS

Matthew J. Gridley, B.S.E.E.
Captain, USAF

Committee:

Maj Milo W. Hyde IV, PhD (Chairman)

Michael A. Marciniak, PhD (Member)

Mark F. Spencer, PhD (Member)

AFIT-ENG-MS-15-M-058

Abstract

The purpose of this research effort is to experimentally generate an electromagnetic Gaussian Schell-model beam from two coherent linearly polarized plane waves. The approach uses a sequence of mutually correlated random phase screens on phase-only liquid crystal spatial light modulators at the source plane. The phase screens are generated using a published relationship between the screen parameters and the desired electromagnetic Gaussian Schell-model source parameters. The approach is verified by comparing the experimental results with published theory and numerical simulation results. This work enables the design of an electromagnetic Gaussian Schell-model source with prescribed coherence and polarization properties.

Acknowledgments

I would like to express my sincere appreciation to my family and friends for their continued support, encouragement, and understanding. I would also like to thank my AFIT professors, especially my research advisor, Major Milo Hyde, for not only imparting their knowledge and instruction, but also for sharing the pain, having patience with me, and keeping me on track throughout my Master's program and research process.

Matthew J. Gridley

Table of Contents

Page

Abstract iv

Acknowledgments v

Table of Contents vi

List of Figures viii

List of Tables xi

List of Acronyms xii

I. Introduction 1

1.1 Research Objective 2
1.2 Limitations 2
1.3 Implications 2
1.4 Preview 3

II. Background 4

2.1 Coherence 4
2.1.1 Mutual Coherence Function 4
2.1.2 Complex Degree of Coherence 5
2.1.3 Cross-Spectral Density 5
2.1.4 Spectral Degree of Coherence 6
2.1.5 Gaussian Schell-Model Source 6
2.1.6 Cross-Spectral Density Matrix 7
2.2 Polarization 8
2.3 Electromagnetic Gaussian Schell-Model Beam Theory 9

III. Methodology 12

3.1 Electromagnetic Gaussian Schell-Model Source Generation 12
3.2 Phase Screen Generation 15
3.3 Spatial Light Modulators 17
3.3.1 Principles of Operation 17
3.3.2 Phase Response Calibration 18

Page

3.3.3 Static Aberration Calibration 23
3.3.4 Comparison of Results 27
3.4 System Model 31
3.4.1 Design 31
3.4.2 Polarization Analyzer 35
3.4.3 Data Collected 35

IV. Analysis and Results 39

4.1 Experiment I Results 41
4.2 Experiment II Results 48

V. Conclusions and Recommendations 55

5.1 Conclusions of Research 55
5.2 Recommendations for Future Research 55

Bibliography 57

List of Figures

Figure Page

3.1 Schematic illustration of system setup for linear phase response calibration. . . 19

3.2 Linear phase response calibration plots for SLM 1 using manufacturer provided look-up-table showing (a) measured irradiance with and without a quarter-wave plate and (b) the unwrapped phase. 21

3.3 Linear phase response calibration plots for SLM 2 using manufacturer provided look-up-table showing (a) measured irradiance with and without a quarter-wave plate and (b) the unwrapped phase. 22

3.4 Pade fit to manufacturer provided look-up-table data for SLM 1 and SLM 2. . . 23

3.5 Modified Gerchberg-Saxton algorithm flow chart for iterative Fourier transform calibration method. 25

3.6 Schematic illustration of system setup for static phase aberration calibration for Path 1. 26

3.7 Schematic illustration of system setup for static phase aberration calibration for Path 2. 26

3.8 Static phase aberration estimates for (a) SLM 1 and (b) SLM 2. 28

3.9 Static aberration calibration diffraction patterns showing a flat phase applied to SLM 1 and propagated through the system to the observation plane (a) without correction applied for the static aberration and (b) with correction applied for the static aberration. 29

3.10 Static aberration calibration diffraction patterns showing a flat phase applied to SLM 2 and propagated through the system to the observation plane (a) without correction applied for the static aberration and (b) with correction applied for the static aberration. 30

Figure Page

3.11 Schematic illustration of experiment design to generate an EGSM source. . . . 31

3.12 Exploded view of lens systems on Path 1 and Path 2 of the experiment design highlighting the translated SLM planes and lens focal lengths. 33

3.13 Schematic illustration of polarization state analyzer composed of a focusing lens, quarter-wave plate, linear polarizer, and imaging camera. 35

4.1 Experiment I Stokes parameter results compared with simulation and theory. The rows are S_0, S_1, S_2, and S_3, respectively, while the columns are the theory, simulation, and experimental results, respectively. 42

4.2 Experiment I Stokes parameter results compared with simulation and theory. The theory, simulation, and experiment slices plotted together for each of (a) S_0, (b) S_1, (c) S_2, and (d) S_3. 43

4.3 Experiment I degree of polarization results for theory, simulation, and experiment. 44

4.4 Experiment I irradiance correlation function results compared with simulation and theory. The rows are $\langle I_x(x_1, y_1)I_x(x_2, y_2)\rangle$, $\langle I_x(x_1, y_1)I_x(x_2, y_2)\rangle$, $\langle I_x(x_1, y_1)I_x(x_2, y_2)\rangle$, and $\langle I_x(x_1, y_1)I_x(x_2, y_2)\rangle$, respectively, while the columns are the theory, simulation, and experimental results, respectively. 46

4.5 Experiment I irradiance correlation function results compared with simulation and theory. The theory, simulation, and experiment slices plotted together for each of (a) $\langle I_x(x_1, y_1)I_x(x_2, y_2)\rangle$, (b) $\langle I_x(x_1, y_1)I_y(x_2, y_2)\rangle$, (c) $\langle I_y(x_1, y_1)I_x(x_2, y_2)\rangle$, and (d) $\langle I_y(x_1, y_1)I_y(x_2, y_2)\rangle$. 47

4.6 Experiment II Stokes parameter results compared with simulation and theory. The rows are S_0, S_1, S_2, and S_3, respectively, while the columns are the theory, simulation, and experimental results, respectively. 49

Figure Page

4.7 Experiment II Stokes parameter results compared with simulation and theory. The theory, simulation, and experiment slices plotted together for each of (a) S_0, (b) S_1, (c) S_2, and (d) S_3. 50

4.8 Experiment II degree of polarization results for theory, simulation, and experiment. 51

4.9 Experiment II irradiance correlation function results compared with simulation and theory. The rows are $\langle I_x(x_1, y_1)I_x(x_2, y_2)\rangle$, $\langle I_x(x_1, y_1)I_x(x_2, y_2)\rangle$, $\langle I_x(x_1, y_1)I_x(x_2, y_2)\rangle$, and $\langle I_x(x_1, y_1)I_x(x_2, y_2)\rangle$, respectively, while the columns are the theory, simulation, and experimental results, respectively. 53

4.10 Experiment II irradiance correlation function results compared with simulation and theory. The theory, simulation, and experiment slices plotted together for each of (a) $\langle I_x(x_1, y_1)I_x(x_2, y_2)\rangle$, (b) $\langle I_x(x_1, y_1)I_y(x_2, y_2)\rangle$, (c) $\langle I_y(x_1, y_1)I_x(x_2, y_2)\rangle$, and (d) $\langle I_y(x_1, y_1)I_y(x_2, y_2)\rangle$. 54

List of Tables

Table Page

3.1 Polarization Analyzer Orientations 36

4.1 EGSM Source Parameters 40

4.2 EGSM Phase Screen Parameters 40

List of Acronyms

Acronym	Definition
BNS	Boulder Nonlinear Systems
CSD	cross-spectral density
CSDM	cross-spectral density matrix
CDoC	complex degree of coherence
DoC	degree of coherence
DoP	degree of polarization
EGSM	electromagnetic Gaussian Schell-model
FOCF	fourth-order correlation function
GAF	Gaussian amplitude filter
GSM	Gaussian Schell-model
HWP	half-wave plate
LC	liquid crystal
LCoS	liquid crystal on silicon
LP	linear polarizer
LUT	look-up-table
MCF	mutual coherence function
PBS	polarizing beam splitter
PSD	power spectral density
QWP	quarter-wave plate
SDoC	spectral degree of coherence
SM	Schell-model
SLM	spatial light modulator
VR	variable retarder

EXPERIMENTAL METHOD OF GENERATING ELECTROMAGNETIC GAUSSIAN SCHELL-MODEL BEAMS

I. Introduction

Electromagnetic Gaussian Schell-model (EGSM) beams use vector theory and have been proposed only recently within the literature [15]. With that said, EGSM beams are a natural extension from Gaussian Schell-model (GSM) beams which use scalar theory [7, 9]. When considering EGSM beams, interesting coherence and polarization properties have been revealed [21]. During propagation a reduction in scintillation has been observed as well as changes in the state of polarization. Due to these observations, EGSM beams have attracted special attention for the potential use in free-space optical communications, imaging through turbulence, and remote sensing applications [11, 17, 18]. Improved performance of the aforementioned applications drives research on this subject and requires the ability to control the attributes of EGSM sources [2].

Theory has greatly improved in understanding EGSM beams over the last few decades. Their propagation aspects, correlation and polarization properties, and realizability conditions are well studied and documented [8, 16, 24, 25]. Current research efforts include analytical and experimental methods proposed to produce EGSM sources [1, 12–15, 21, 23, 26]. Many of the proposed methods of generation are based on interferometer designs and may use either rotating phase wheels, ground glass diffusers, or a more practical design based around a liquid crystal (LC) spatial light modulator (SLM) [15, 21]. There are proposed methods and experimental designs for measuring the EGSM beam parameters [12, 23]. The most recent successful experiment demonstrated a reduction in scintillation of a completely unpolarized EGSM beam propagated through simulated

atmospheric turbulence [1]. Practical techniques are all shown by the above research efforts to generate an EGSM beam and work together to validate the existing theory; however, these efforts do not focus on the ability to generate an EGSM beam with desired characteristics.

1.1 Research Objective

The objective of this research effort is to design an experiment with the capability to generate an EGSM beam with prescribed coherence and polarization properties from two coherent linearly polarized plane waves. The experimental design will utilize a pair of phase-only nematic LC SLMs which will display a sequence of mutually correlated random phase screens. As such, the desired EGSM source parameters dictate the required screen parameters [2]. The random phase screens will then be generated with the required parameters from the relationship, and the experimental results will be verified by comparison to published theory and computational simulation results [2, 17].

1.2 Limitations

Many variables are involved in the ability to generate an EGSM source experimentally. Most of the limitations in this effort derive from time allotted to complete the experiment; however, there are limitations due to resources. Many of the optical laboratory resources used in the construction of the system will be on-hand equipment due to the often prohibitive cost or time necessary to acquire new equipment. This brings about limitations due to age or quality of the equipment. Ultimately without more time, there will be equipment not calibrated and the full capability of the experiment design will not be verified. This will be evident when compared to results seen in theory and simulation.

1.3 Implications

Results from this research effort could feasibly be applied directly to free space optical communications, imaging through turbulence, remote sensing, or directed energy

programs. If improvements in the electro-optical components and optical elements are made, or advancements in the use of the SLMs are undertaken, the experimental results could be improved greatly allowing for further research and possible application in the aforementioned programs.

1.4 Preview

The experimental research presented here aims to demonstrate that an EGSM source can be generated with the desired coherence and polarization properties with high fidelity and configurability. Chapter 2, Literature Review, discusses the knowledge base necessary for the understanding of EGSM sources, generation, and propagation. Chapter 3, Methodology, details the computational methodology that led to the experimental design, as well as the approach to constructing the experiment. Chapter 4, Analysis and Results, interprets the gathered theoretical, simulated, and experimental data. Chapter 5, Conclusions and Recommendations, discusses the validity and performance of the experiment based on comparisons of the theoretical, simulated, and experimental results.

II. Background

All optical fields undergo random fluctuations. They may be small, as in the output of many lasers, or they may be appreciably larger as in light generated by thermal sources. The underlying theory of fluctuating optical fields is known as coherence theory. An important manifestation of the fluctuations is the phenomenon of partial coherence and partial polarization. Unlike usual treatments it describes optical fields in terms of observable quantities and elucidates how such quantities change as light propagates [24]. This background information provides a unified treatment of the phenomena of coherence and polarization. Chapter 2 discusses the theory behind coherence and polarization, which are of considerable importance with the propagation of EGSM beams, as well as discussing the theory behind EGSM beams.

2.1 Coherence

In a given random field, coherence describes the degree to which one point relates to any other point in the field in time or space. Coherence is realized mathematically through the correlation function $\Gamma(\mathbf{r}_1, \mathbf{r}_2; t_1, t_2)$. The correlation function Γ depends on two points in space ($\mathbf{r}_1$ and $\mathbf{r}_2$) or two instances in time (t_1 and t_2).

2.1.1 Mutual Coherence Function.

In second-order coherence theory, Wolf, Goodman, and others present the mutual coherence function (MCF) $\Gamma(\mathbf{r}_1, \mathbf{r}_2, \tau)$ which is valuable in analyzing spatial coherence [6, 25]. Specifically,

$$\Gamma(\mathbf{r}_1, \mathbf{r}_2, \tau) = \langle u(\mathbf{r}_1, t + \tau) u^*(\mathbf{r}_2, t) \rangle, \tag{2.1}$$

which is a time auto-correlation of an analytic function $u(\mathbf{r}, t)$ at two points in space ($\mathbf{r}_1$ and $\mathbf{r}_2$). Equation (2.1) reduces to a self-coherence function when only a single point in

space $\mathbf{r}$ is analyzed. An assumption must be made when using Eq. (2.1) that the field is at least wide-sense stationary, i.e., the average field has no explicit time dependence [25].

2.1.2 Complex Degree of Coherence.

The complex degree of coherence (CDoC) $\gamma(\mathbf{r}_1, \mathbf{r}_2, \tau)$ is acquired by normalizing the MCF as shown in Eq. (2.1), where

$$\gamma(\mathbf{r}_1, \mathbf{r}_2, \tau) = \frac{\Gamma(\mathbf{r}_1, \mathbf{r}_2, \tau)}{\sqrt{\Gamma(\mathbf{r}_1, \mathbf{r}_1, \tau)\Gamma(\mathbf{r}_2, \mathbf{r}_2, \tau)}}. \tag{2.2}$$

A normalized unit of measure is given by the magnitude of the CDoC for the amount of temporal or spatial coherence of a field for two points in space, $\mathbf{r}_1$ and $\mathbf{r}_2$, and a time difference $\tau = t_2 - t_1$. The field is considered fully coherent if $|\gamma(\mathbf{r}_1, \mathbf{r}_2, \tau)| = 1$, i.e., two different points in space are correlated. Conversely, the field is considered fully incoherent if $|\gamma(\mathbf{r}_1, \mathbf{r}_2, \tau)| = 0$, i.e., two points in space are uncorrelated. A field that measures $0 < |\gamma(\mathbf{r}_1, \mathbf{r}_2, \tau)| < 1$ is considered partially coherent.

2.1.3 Cross-Spectral Density.

The cross-spectral density (CSD) $W(\mathbf{r}_1, \mathbf{r}_2, \omega)$ is another way of analyzing spatial coherence [25]. The CSD and MCF form a Fourier transform pair given by

$$\Gamma(\mathbf{r}_1, \mathbf{r}_2, \tau) = \frac{1}{2\pi} \int_0^\infty W(\mathbf{r}_1, \mathbf{r}_2, \omega) \exp(\mathrm{j}\,\omega\tau) \mathrm{d}\tau. \tag{2.3}$$

This demonstrates the ability to analyze spatial coherence in the space-frequency domain with the CSD as opposed to the space-time domain with the MCF. The following result, derived by Wolf [25],

$$W(\mathbf{r}_1, \mathbf{r}_2, \omega) = \langle U(\mathbf{r}_1, \omega) U^*(\mathbf{r}_2, \omega) \rangle, \tag{2.4}$$

shows the CSD is the auto-correlation function of an ensemble of sample functions $\{U(\mathbf{r}, \omega)\}$. With the use of the Wiener-Khinchin theorem, the autocorrelation and spectral density form the Fourier transform pair for a zero-mean, wide-sense stationary random process [6, 25].

2.1.4 Spectral Degree of Coherence.

Normalizing the CSD as given in Eq. (2.4), generates the spectral degree of coherence (SDoC) $\mu(\mathbf{r}_1, \mathbf{r}_2, \omega)$, where

$$\mu(\mathbf{r}_1, \mathbf{r}_2, \omega) = \frac{W(\mathbf{r}_1, \mathbf{r}_2, \omega)}{\sqrt{W(\mathbf{r}_1, \mathbf{r}_1, \omega)W(\mathbf{r}_2, \mathbf{r}_2, \omega)}}. \tag{2.5}$$

A normalized unit of measure is given by the magnitude of the SDoC for the amount of spatial coherence of a field for two points in space, $\mathbf{r}_1$ and $\mathbf{r}_2$, and angular frequency ω. Two different points in space are correlated if $|\mu(\mathbf{r}_1, \mathbf{r}_2, \omega)| = 1$ and the field is considered spatially coherent; conversely, two points in space are uncorrelated if $|\mu(\mathbf{r}_1, \mathbf{r}_2, \omega)| = 0$ and the field is considered spatially incoherent. A field that measures $0 < |\mu(\mathbf{r}_1, \mathbf{r}_2, \omega)| < 1$ is considered spatially partially coherent.

2.1.5 Gaussian Schell-Model Source.

In the source plane of the field at the origin, the CSD is structured as

$$W(\boldsymbol{\rho}_1, \boldsymbol{\rho}_2, \omega) = \langle U(\boldsymbol{\rho}_1, \omega)U^*(\boldsymbol{\rho}_2, \omega)\rangle, \tag{2.6}$$

where $\boldsymbol{\rho}_{1,2} = x_{1,2}\hat{\boldsymbol{x}} + y_{1,2}\hat{\boldsymbol{y}}$. Accordingly, the CSD $W(\boldsymbol{\rho}_1, \boldsymbol{\rho}_2, \omega)$ of a GSM source is structured as [25]

$$\begin{aligned} W(\boldsymbol{\rho}_1, \boldsymbol{\rho}_2, \omega) &= \sqrt{S(\boldsymbol{\rho}_1, \omega)}\sqrt{S(\boldsymbol{\rho}_2, \omega)}\mu(\boldsymbol{\rho}_2 - \boldsymbol{\rho}_1, \omega) \\ S(\boldsymbol{\rho}, \omega) &= A^2 \exp\left(-\frac{|\boldsymbol{\rho}|^2}{2w^2}\right) \\ \mu(\boldsymbol{\rho}, \omega) &= \exp\left(-\frac{|\boldsymbol{\rho}|^2}{2\ell^2}\right) \end{aligned} . \tag{2.7}$$

Parameters A^2, w, and ℓ are space independent but are dependent on angular frequency ω. When Eq. (2.7) is substituted into Eq. (2.5), the magnitude of the SDoC becomes

$$|\mu(\boldsymbol{\rho}_2 - \boldsymbol{\rho}_1, \omega)| = \exp\left(-\frac{|\boldsymbol{\rho}_2 - \boldsymbol{\rho}_1|^2}{2\ell^2}\right), \tag{2.8}$$

which is only dependent on the distance between two points and not the points themselves [25].

The source coherence length ℓ is the distance between two points $|\boldsymbol{\rho}_2 - \boldsymbol{\rho}_1|$ where the magnitude of the SDoC falls to $1/e^2$ of its original on-axis value. This is a direct result of the relationship found in Eq. (2.8). The GSM source is spatially coherent and the two points are correlated if $|\boldsymbol{\rho}_2 - \boldsymbol{\rho}_1| \ll \ell$; however, the GSM source is spatially incoherent and the two points are uncorrelated if $|\boldsymbol{\rho}_2 - \boldsymbol{\rho}_1| \gg \ell$. The GSM source is partially spatially coherent if $0 < |\boldsymbol{\rho}_2 - \boldsymbol{\rho}_1| < \ell$.

2.1.6 Cross-Spectral Density Matrix.

The cross-spectral density matrix (CSDM) $\mathbf{W}(\mathbf{r}_1, \mathbf{r}_2, \omega)$ is utilized for the analysis of spatial coherence of electromagnetic vector fields in the space-frequency domain [25]. The CSDM is the outer product generated from electric field vectors of the following form:

$$\begin{aligned} \boldsymbol{E}(\boldsymbol{\rho}, \omega) &= E_x(\boldsymbol{\rho}, \omega)\hat{\boldsymbol{x}} + E_y(\boldsymbol{\rho}, \omega)\hat{\boldsymbol{y}} \\ &= \begin{pmatrix} E_x(\boldsymbol{\rho}, \omega) \\ E_y(\boldsymbol{\rho}, \omega) \end{pmatrix} \end{aligned} , \tag{2.9}$$

such that

$$\begin{aligned} \mathbf{W}(\boldsymbol{\rho}_1, \boldsymbol{\rho}_2, \omega) \equiv& \langle \boldsymbol{E}(\boldsymbol{\rho}_1, \omega)\boldsymbol{E}^H(\boldsymbol{\rho}_2, \omega)\rangle \\ =& \left\langle \begin{pmatrix} E_x(\boldsymbol{\rho}_1, \omega) \\ E_y(\boldsymbol{\rho}_2, \omega) \end{pmatrix} \begin{pmatrix} E_x^*(\boldsymbol{\rho}_1, \omega) & E_y^*(\boldsymbol{\rho}_2, \omega) \end{pmatrix} \right\rangle \\ =& \left\langle \begin{pmatrix} E_{x1} \\ E_{y1} \end{pmatrix} \begin{pmatrix} E_{x2}^* & E_{y2}^* \end{pmatrix} \right\rangle \\ =& \begin{pmatrix} \langle E_{x1}E_{x2}^*\rangle & \langle E_{x1}E_{y2}^*\rangle \\ \langle E_{y1}E_{x2}^*\rangle & \langle E_{y1}E_{y2}^*\rangle \end{pmatrix} \end{aligned} , \tag{2.10}$$

and

$$W_{\alpha\beta}(\boldsymbol{\rho}_1, \boldsymbol{\rho}_2, \omega) = \langle E_\alpha(\boldsymbol{\rho}_1, \omega)E_\beta^*(\boldsymbol{\rho}_2, \omega)\rangle \qquad \begin{pmatrix} \alpha = x, y \\ \beta = x, y \end{pmatrix}, \tag{2.11}$$

where ^{H} denotes Hermitian conjugate. In Eq. (2.9), $E_x(\boldsymbol{\rho}, \omega)$ and $E_y(\boldsymbol{\rho}, \omega)$ are analytic functions in two mutually orthogonal directions perpendicular to the direction of propagation.

Accordingly, the SDoC is determined from the CSDM using the following relationship [25]:

$$\mu(\boldsymbol{\rho}_1, \boldsymbol{\rho}_2, \omega) = \frac{\mathrm{Tr}\{\mathbf{W}(\boldsymbol{\rho}_1, \boldsymbol{\rho}_2, \omega)\}}{\sqrt{\mathrm{Tr}\{\mathbf{W}(\boldsymbol{\rho}_1, \boldsymbol{\rho}_1, \omega)\}}\sqrt{\mathrm{Tr}\{\mathbf{W}(\boldsymbol{\rho}_2, \boldsymbol{\rho}_2, \omega)\}}}, \tag{2.12}$$

where $\mathrm{Tr}\{\cdots\}$ denotes the trace. Formulated with electromagnetic vector fields, a normalized unit of measure is given by the magnitude of the SDoC for the degree of spatial coherence, i.e., $0 \leq |\mu(\boldsymbol{\rho}_1, \boldsymbol{\rho}_2, \omega)| \leq 1$.

The CSDM of a GSM source takes the following element-based form [25]:

$$\begin{gathered} W_{\alpha\beta}(\boldsymbol{\rho}_1, \boldsymbol{\rho}_2, \omega) = \sqrt{S_\alpha(\boldsymbol{\rho}_1, \omega)}\sqrt{S_\beta(\boldsymbol{\rho}_2, \omega)}\mu(\boldsymbol{\rho}_2 - \boldsymbol{\rho}_1, \omega) \\ S_m(\boldsymbol{\rho}, \omega) = A_\alpha^2 \exp\left(-\frac{|\boldsymbol{\rho}|^2}{2w_\alpha^2}\right) \\ \mu_{\alpha\beta}(\boldsymbol{\rho}_2 - \boldsymbol{\rho}_1, \omega) = B_{\alpha\beta} \exp\left(-\frac{|\boldsymbol{\rho}_2 - \boldsymbol{\rho}_1|^2}{2\ell_{\alpha\beta}^2}\right) \\ (\alpha = x, y \text{ and } \beta = x, y) \end{gathered} . \tag{2.13}$$

Element-based parameters A_α^2, $B_{\alpha\beta}$, w_α, and $\ell_{\alpha\beta}$ are space independent but are dependent on angular frequency ω.

2.2 Polarization

Given electromagnetic vector fields and the CSDM as defined in Eq. (2.10), the following relationships of interest exist for polarization. The first relationship of interest is the space- and angular-frequency-dependent degree of polarization (DoP) $P(\boldsymbol{\rho}, \omega)$ [25]. Specifically,

$$P(\boldsymbol{\rho}, \omega) = \sqrt{1 - \frac{4\mathrm{Det}\{\mathbf{W}(\boldsymbol{\rho}, \boldsymbol{\rho}, \omega)\}}{(\mathrm{Tr}\{\mathbf{W}(\boldsymbol{\rho}, \boldsymbol{\rho}, \omega)\})^2}}, \tag{2.14}$$

where, $\mathrm{Det}\{\cdots\}$ denotes the determinant operation. A normalized unit of measure is given by the DoP for the amount of polarization in a field [25]. The field is polarized when $P(\boldsymbol{\rho}, \omega) = 1$; conversely, the field is unpolarized when $P(\boldsymbol{\rho}, \omega) = 0$. The field is partially polarized when $0 < P(\boldsymbol{\rho}, \omega) < 1$.

The last relationship of interest is the single point Stokes vector $S_l(\boldsymbol{\rho}, \omega)$, where $l = 1, 2, 3, 4$. The components of this vector are

$$\begin{aligned} S_0(\boldsymbol{\rho}, \omega) =& W_{xx}(\boldsymbol{\rho}, \boldsymbol{\rho}, \omega) + W_{yy}(\boldsymbol{\rho}, \boldsymbol{\rho}, \omega) \\ S_1(\boldsymbol{\rho}, \omega) =& W_{xx}(\boldsymbol{\rho}, \boldsymbol{\rho}, \omega) - W_{yy}(\boldsymbol{\rho}, \boldsymbol{\rho}, \omega) \\ S_2(\boldsymbol{\rho}, \omega) =& W_{xy}(\boldsymbol{\rho}, \boldsymbol{\rho}, \omega) + W_{yx}(\boldsymbol{\rho}, \boldsymbol{\rho}, \omega) \\ S_3(\boldsymbol{\rho}, \omega) =& \mathrm{j}\left[W_{yx}(\boldsymbol{\rho}, \boldsymbol{\rho}, \omega) - W_{xy}(\boldsymbol{\rho}, \boldsymbol{\rho}, \omega)\right] \end{aligned} . \tag{2.15}$$

The Stokes vector is useful in analyzing polarization [25]. Utilizing the Stokes vector, the DoP is

$$P(\boldsymbol{\rho}, \omega) = \frac{\sqrt{S_1^2(\boldsymbol{\rho}, \omega) + S_2^2(\boldsymbol{\rho}, \omega) + S_3^2(\boldsymbol{\rho}, \omega)}}{S_0(\boldsymbol{\rho}, \omega)}, \tag{2.16}$$

which demonstrates a second method within the analysis.

2.3 Electromagnetic Gaussian Schell-Model Beam Theory

Now that the fundamental theory has been covered, the theoretical solution developed by Korotkova and Hyde for the generation of the EGSM beam is reviewed [2, 17]. Korotkova's method uses the tensor technique to characterize the source. The following analysis presents the key equations from Korotkova's derivation that are necessary for analytical comparison of the EGSM source plane [17].

Beginning in the source plane, the tensor notation for each of the four CSDM elements of the EGSM have the form

$$\begin{gathered} W_{\alpha\beta}(\tilde{\mathbf{r}}, 0) = A_\alpha A_\beta B_{\alpha\beta} \exp\left[-\frac{\mathrm{j}k}{2}\tilde{\mathbf{r}}^T \mathbf{M}_{0\alpha\beta}^{-1}\tilde{\mathbf{r}}\right], \\ (\alpha = x, y \text{ and } \beta = x, y) \end{gathered} \tag{2.17}$$

where $\tilde{\mathbf{r}}$ is the 4×4 vector such that $\tilde{\mathbf{r}} = (\mathbf{r}_1, \mathbf{r}_2)$, $\mathbf{r}_1$ and $\mathbf{r}_2$ are two-dimensional vectors in the source plane, k is the wave number, and $\mathbf{M}_{0\alpha\beta}^{-1}$ is the 4×4 matrix expressed as

$$\mathbf{M}_{0\alpha\beta}^{-1} = \begin{pmatrix} \frac{1}{\mathrm{j}k}\left(\frac{1}{2\sigma_\alpha^2} + \frac{1}{\delta_{\alpha\beta}^2}\right)\mathbf{I} & \frac{\mathrm{j}}{k\delta_{\alpha\beta}^2}\mathbf{I} \\ \frac{\mathrm{j}}{k\delta_{\alpha\beta}^2}\mathbf{I} & \frac{1}{\mathrm{j}k}\left(\frac{1}{2\sigma_\beta^2} + \frac{1}{\delta_{\alpha\beta}^2}\right)\mathbf{I} \end{pmatrix}. \tag{2.18}$$

Parameters A_α, $B_{\alpha\beta}$, σ_α, and $\delta_{\alpha\beta}$ in Eq. (2.17) are independent of position but depend on frequency, and $\mathbf{I}$ is the identity matrix.

The above detailed equations provide the theoretical solution for comparison of an EGSM beam in the source plane. Now that the source plane is derived, the theoretical solution by Hyde for an EGSM beam propagated through a lens to the observation plane is reviewed. The following are the key equations.

Each of the four CSDM elements of the EGSM beam in the source plane have the form

$$\begin{aligned}
W_{\alpha\beta}(\boldsymbol{\rho}_1', \boldsymbol{\rho}_2', 0^-) =& A_\alpha A_\beta B_{\alpha\beta} \exp\left[-\frac{\rho_1'^2}{4\sigma_\alpha^2}\right] \exp\left[-\frac{\rho_2'^2}{4\sigma_\beta^2}\right] \exp\left[-\frac{|\boldsymbol{\rho}_1' - \boldsymbol{\rho}_2'|^2}{2\delta_{\alpha\beta}^2}\right] \\
W_{\alpha\beta}(\boldsymbol{\rho}_1, \boldsymbol{\rho}_2, f) =& A_\alpha A_\beta B_{\alpha\beta} \frac{1}{(\lambda f)^2} \exp\left[\frac{\mathrm{j}k}{2f}(\rho_1^2 - \rho_2^2)\right] \iiiint \exp\left[-\frac{\rho_1'^2}{4\sigma_\alpha^2}\right] \exp\left[-\frac{\rho_2'^2}{4\sigma_\beta^2}\right], \\
& \exp\left[-\frac{|\boldsymbol{\rho}_1' - \boldsymbol{\rho}_2'|^2}{2\delta_{\alpha\beta}^2}\right] \exp\left[-\frac{\mathrm{j}k}{f}(\boldsymbol{\rho}_1\boldsymbol{\rho}_1' - \boldsymbol{\rho}_2\boldsymbol{\rho}_2')\right] \mathrm{d}^2\rho_1' \mathrm{d}^2\rho_2' \\
& (\alpha = x, y \text{ and } \beta = x, y)
\end{aligned} \tag{2.19}$$

where $z = 0^-$ is the source plane directly before the lens and $z = f$ is the focal plane of the lens, i.e., the observation plane.

After evaluating the integrals, the four CSDM elements of the EGSM beam are

$$\begin{aligned}
W_{\alpha\beta}(\boldsymbol{\rho}_1, \boldsymbol{\rho}_2, f) =& \frac{A_\alpha A_\beta B_{\alpha\beta}\pi^2}{a_{\alpha,\alpha\beta}a_{\beta,\alpha\beta} - b_{\alpha\beta}^2} \frac{1}{(\lambda f)^2} \exp\left[\frac{\mathrm{j}k}{2f}(x_1^2 + y_1^2)\right] \exp\left[-\frac{\mathrm{j}k}{2f}(x_2^2 + y_2^2)\right] \\
& \exp\left[-\frac{k^2}{4f^2}\left(\frac{a_{\beta,\alpha\beta}x_1^2 - 2b_{\alpha\beta}x_1x_2 + a_{\alpha,\alpha\beta}x_2^2}{a_{\alpha,\alpha\beta}a_{\beta,\alpha\beta} - b_{\alpha\beta}^2}\right)\right] \\
& \exp\left[-\frac{k^2}{4f^2}\left(\frac{a_{\beta,\alpha\beta}y_1^2 - 2b_{\alpha\beta}y_1y_2 + a_{\alpha,\alpha\beta}y_2^2}{a_{\alpha,\alpha\beta}a_{\beta,\alpha\beta} - b_{\alpha\beta}^2}\right)\right] \\
& (\alpha = x, y \text{ and } \beta = x, y)
\end{aligned}, \tag{2.20}$$

where

$$
\begin{aligned}
a_{\alpha,\alpha\beta} &= \frac{1}{4\sigma_{\alpha}^{2}} + \frac{1}{2\delta_{\alpha\beta}^{2}} \\
a_{\beta,\alpha\beta} &= \frac{1}{4\sigma_{\beta}^{2}} + \frac{1}{2\delta_{\alpha\beta}^{2}}, \\
b_{\alpha\beta} &= \frac{1}{2\delta_{\alpha\beta}^{2}}
\end{aligned}
\tag{2.21}
$$

and

$$
\begin{aligned}
\rho_{1}^{2} &= \left(x_{1}^{2} + y_{1}^{2}\right) \\
\rho_{1}^{2} &= \left(x_{2}^{2} + y_{2}^{2}\right)
\end{aligned}.
\tag{2.22}
$$

The above detailed equations provide the theoretical solution for comparison of an EGSM beam in the observation plane.

III. Methodology

Chapter 3 discusses a published method of numerically generating an EGSM source with prescribed coherence and polarization properties and the relationships between the EGSM source and phase screen parameters. These relationships provide the basis for creating the phase screens necessary to experimentally generate an EGSM source. Further, the experimental design will be discussed in detail, to include the calibration of the SLMs and the collection and measurement of data.

3.1 Electromagnetic Gaussian Schell-Model Source Generation

With a theoretical solution for comparison, the method for creating an EGSM source must be detailed. The following method to create the source was developed by Hyde and the key equations, steps, and much of the derivation are reproduced in the following section [2]. The following analysis uses the EGSM source CSDM from Wolf as shown in Eq. (2.13)

and reproduced here for convenience, i.e., [25]:

$$
\begin{gathered}
W_{ij}(\boldsymbol{\rho}_1, \boldsymbol{\rho}_2, 0, \omega) = \sqrt{S_i(\boldsymbol{\rho}_1; \omega)}\sqrt{S_j(\boldsymbol{\rho}_2; \omega)} \\
\mu_{ij}(|\boldsymbol{\rho}_1 - \boldsymbol{\rho}_2|; \omega) \quad (i = x, y \;\; j = x, y) \\
S_i(\boldsymbol{\rho}; \omega) = A_i^2 \exp\left(\frac{-\rho^2}{2\sigma_i^2}\right) \\
\mu_{ij}(|\boldsymbol{\rho}_1 - \boldsymbol{\rho}_2|; \omega) = B_{ij} \exp\left(\frac{-|\boldsymbol{\rho}_1 - \boldsymbol{\rho}_2|^2}{2\delta_{ij}^2}\right) \\
B_{ij} = 1 \quad i = j \\
|B_{ij}| \leq 1 \quad i \neq j \\
B_{ij} = B_{ij}^* \\
\delta_{ij} = \delta_{ji} \\
\sqrt{\frac{\delta_{xx}^2 + \delta_{yy}^2}{2}} \leq \delta_{xy} \leq \sqrt{\frac{\delta_{xx}\delta_{yy}}{|B_{xy}|}} \quad [8] \\
\frac{1}{4\sigma_i^2} + \frac{1}{\delta_{ii}^2} \ll \frac{2\pi^2}{\lambda^2}
\end{gathered}
\tag{3.1}
$$

The next step in the analysis is to define the electric field [reference Eq. (2.9)] in the source plane, i.e., $z = 0$, as

$$
E_\alpha(\boldsymbol{\rho}) = C_\alpha \exp\left(\frac{-\rho^2}{4\sigma_\alpha^2}\right) \exp\left[\mathrm{j}\phi_\alpha(\boldsymbol{\rho})\right] \quad (\alpha = x, y), \tag{3.2}
$$

where $C_\alpha = |C_\alpha| \exp(\mathrm{j}\,\theta_\alpha)$ is a complex constant. Performing the autocorrelations necessary to fill the CSDM in Eq. (2.10) produces

$$
\langle E_{\alpha 1} E_{\beta 2}^* \rangle = C_\alpha C_\beta^* \exp\left[-\left(\frac{\rho_1^2}{4\sigma_\alpha^2} + \frac{\rho_2^2}{4\sigma_\alpha^2}\right)\right] \langle \exp[\mathrm{j}\phi_\alpha(\boldsymbol{\rho}_1)] \exp[-\mathrm{j}\phi_\beta(\boldsymbol{\rho}_2)] \rangle \qquad \begin{pmatrix} \alpha = x, y \\ \beta = x, y \end{pmatrix}, \tag{3.3}
$$

where ϕ_α and ϕ_β are random phase screens. These phase screens are sample functions drawn from two correlated Gaussian random processes which are detailed in the next section.

To allow for the approximation of the normalized cross-correlation function, the function is taken to be Gaussian-shaped and the standard deviations of the phase screens,

σ_{ϕ_α} and σ_{ϕ_β}, are assumed to be greater than π. This yields

$$\langle \exp[\mathrm{j}\phi_{\alpha 1}]\exp[-\mathrm{j}\phi_{\beta 2}]\rangle \approx \exp\left[-\frac{1}{2}\left(\sigma_{\phi_\alpha}^2 - 2\rho_{\phi_\alpha\phi_\beta}\sigma_{\phi_\alpha}\sigma_{\phi_\beta} + \sigma_{\phi_\beta}^2\right)\right]\exp\left[-\frac{|\boldsymbol{\rho}_1 - \boldsymbol{\rho}_2|^2}{\ell_{\phi_\alpha\phi_\beta}^2/\rho_{\phi_\alpha\phi_\beta}\sigma_{\phi_\alpha}\sigma_{\phi_\beta}}\right], \tag{3.4}$$

where $0 \leq \rho_{\phi_\alpha\phi_\beta} \leq 1$ is a correlation coefficient ($\rho_{\phi_\alpha\phi_\beta} = 1$ if $\alpha = \beta$). Eq. (3.4) is substituted into Eq. (3.3) and simplified to form

$$\begin{aligned}\langle E_{\alpha 1}E_{\beta 2}^*\rangle =& C_\alpha C_\beta^* \exp\left[-\left(\frac{\rho_1^2}{4\sigma_\alpha^2} + \frac{\rho_2^2}{4\sigma_\alpha^2}\right)\right]\exp\left[-\frac{1}{2}\left(\sigma_{\phi_\alpha}^2 - 2\rho_{\phi_\alpha\phi_\beta}\sigma_{\phi_\alpha}\sigma_{\phi_\beta} + \sigma_{\phi_\beta}^2\right)\right] \\ & \exp\left[-\frac{|\boldsymbol{\rho}_1 - \boldsymbol{\rho}_2|^2}{\ell_{\phi_\alpha\phi_\beta}^2/\rho_{\phi_\alpha\phi_\beta}\sigma_{\phi_\alpha}\sigma_{\phi_\beta}}\right].\end{aligned} \tag{3.5}$$

The "self" terms of the CSDM are created by letting $\alpha = \beta = x$ or y, shown for x as follows:

$$\langle E_{x1}E_{x2}^*\rangle = |C_x|^2 \exp\left[-\left(\frac{\rho_1^2 + \rho_2^2}{4\sigma_x^2}\right)\right]\exp\left[-\frac{|\boldsymbol{\rho}_1 - \boldsymbol{\rho}_2|^2}{\ell_{\phi_x\phi_x}^2/\sigma_{\phi_x}^2}\right]. \tag{3.6}$$

Comparing Eq. (3.6) (or the equivalent for $\alpha = \beta = y$) to Wolf's GSM form, the following relationships are required:

$$\begin{aligned}\delta_{xx} =& \frac{1}{\sqrt{2}}\frac{\ell_{\phi_x\phi_x}}{\sigma_{\phi_x}} \qquad & |C_x| = A_x \\ \delta_{yy} =& \frac{1}{\sqrt{2}}\frac{\ell_{\phi_y\phi_y}}{\sigma_{\phi_y}} \qquad & |C_y| = A_y\end{aligned}. \tag{3.7}$$

Similarly, the "cross" terms of the CSDM are produced by letting $\alpha = x$ and $\beta = y$, from which the following relationships are required to match Wolf's GSM form

$$\begin{aligned}\delta_{xy} =& \frac{1}{\sqrt{2}}\frac{\ell_{\phi_x\phi_y}}{\sqrt{\rho_{\phi_x\phi_y}\sigma_{\phi_x}\sigma_{\phi_y}}} \\ |B_{xy}| =& \exp\left[-\frac{1}{2}\left(\sigma_{\phi_x}^2 - 2\rho_{\phi_x\phi_y}\sigma_{\phi_x}\sigma_{\phi_y} + \sigma_{\phi_y}^2\right)\right]\cdot \\ \angle B_{xy} =& \theta_x - \theta_y\end{aligned} \tag{3.8}$$

Further, letting $\alpha = y$ and $\beta = x$ provides the complement relationship to Eq. (3.8), which satisfies Wolf's requirement for B_{ij} and δ_{ij} as defined in Eq. (3.1). As demonstrated in further detail in Ref. [2], the above approach for simulating an EGSM source is analytically sound.

3.2 Phase Screen Generation

Now that the EGSM source has been created, the correlated random phase screens must be generated. As with the previous section for creating a source, the following method for creating the phase screens was completed by Hyde and the key equations and steps are highlighted [2].

Let ϕ and $\tilde{\phi}$ be Fourier transform pairs, i.e.,

$$\begin{aligned} \tilde{\phi}(f_x, f_y) &= \iint_{-\infty}^{\infty} \phi(x, y)\exp(-\mathrm{j}2\pi f_x x)\exp(-\mathrm{j}2\pi f_y y)\mathrm{d}x\mathrm{d}y \\ \phi(x, y) &= \iint_{-\infty}^{\infty} \phi(f_x, f_y)\exp(-\mathrm{j}2\pi f_x x)\exp(-\mathrm{j}2\pi f_y y)\mathrm{d}f_x\mathrm{d}f_y \end{aligned} . \tag{3.9}$$

It must also be noted that the phase screens are zero mean and Gaussian correlated:

$$\begin{aligned} \langle \phi_x(x, y)\rangle = \langle \phi_y(x, y)\rangle = \langle \phi_\alpha(x, y)\rangle = 0 \\ \langle \phi_\alpha(x_1, y_1)\phi_\alpha^*(x_2, y_2)\rangle = \sigma_{\phi_\alpha}^2 \exp\left(-\frac{|\boldsymbol{\rho}_1 - \boldsymbol{\rho}_2|^2}{\ell_{\phi_\alpha\phi_\alpha}^2}\right) \end{aligned} . \tag{3.10}$$

Expanding ϕ_α in a Fourier series and taking the autocorrelation produces

$$\langle \phi_\alpha(x_1, y_1)\phi_\alpha^*(x_2, y_2)\rangle = \sum_{m,n}\sum_{p,q} \langle \varphi_{\alpha mn}\varphi_{\alpha pq}^*\rangle \exp\left[\mathrm{j}\frac{2\pi}{L}(mx_1 - px_2)\right]\exp\left[\mathrm{j}\frac{2\pi}{L}(ny_1 - qy_2)\right], \tag{3.11}$$

where the Fourier series coefficients $\varphi_{\alpha mn}$ and $\varphi_{\alpha pq}$ are zero mean Gaussian random numbers and $L = N\Delta$ is the size of the discrete grid. This expression must equal the autocorrelation of ϕ_α computed using Eq. (3.9), that is,

$$\langle \phi_\alpha(x_1, y_1)\phi_\alpha^*(x_2, y_2)\rangle = \iint_{-\infty}^{\infty} \Phi_{\phi_\alpha\phi_\alpha}(f_x, f_y)\exp\left[\mathrm{j}2\pi f_x(x_1 - x_2)\right]\exp\left[\mathrm{j}2\pi f_y(y_1 - y_2)\right]\mathrm{d}f_x\mathrm{d}f_y, \tag{3.12}$$

where $\Phi_{\phi_\alpha\phi_\alpha}$ is equivalent to the power spectral density (PSD) of ϕ_α:

$$\Phi_{\phi_\alpha\phi_\alpha}(f_x, f_y) = \sigma_{\phi_\alpha}^2 \pi \ell_{\phi_\alpha\phi_\alpha}^2 \exp\left[-\pi^2 \ell_{\phi_\alpha\phi_\alpha}^2 (f_x^2 + f_y^2)\right]. \tag{3.13}$$

The correlation in Eq. (3.12) must be discretized. To do so the integrals must be expanded in Riemann sums. These sums when compared to Eq. (3.11) result in the following relationships:

$$\begin{aligned} \langle \varphi_{\alpha mn} \varphi^*_{\alpha pq} \rangle &= \Phi_{\phi_\alpha \phi_\alpha}\left(\frac{m}{L}, \frac{n}{L}\right) \delta_{mp} \delta_{nq} \frac{1}{L^2} \\ \langle |\varphi_{\alpha mn}|^2 \rangle &= \Phi_{\phi_\alpha \phi_\alpha}\left(\frac{m}{L}, \frac{n}{L}\right) \frac{1}{L^2} \end{aligned}, \tag{3.14}$$

where $\langle |\varphi_{\alpha mn}|^2 \rangle$ is equivalent to the variance of the Fourier series coefficients $\varphi_{\alpha mn}$ and δ_{mp} and δ_{nq} are Kronecker deltas.

Thus, the phase screen ϕ_α can be produced by generating a matrix of unit variance circular complex Gaussian random numbers r_α, multiplying r_α by the square root of Eq. (3.14), and performing a two-dimensional discrete inverse Fourier transform, namely,

$$\begin{aligned} \phi_\alpha[i, j] = \sum_{m,n} r_\alpha[m, n] \frac{\sigma_{\phi_\alpha} \sqrt{\pi} \ell_{\phi_\alpha \phi_\alpha}}{N\Delta} \exp\left\{ -\frac{\pi^2 \ell^2_{\phi_\alpha \phi_\alpha}}{2} \left[\left(\frac{m}{N\Delta}\right)^2 + \left(\frac{n}{N\Delta}\right)^2 \right] \right\} \\ \exp\left(\mathrm{j}\frac{2\pi}{N} mi\right) \exp\left(\mathrm{j}\frac{2\pi}{N} nj\right). \end{aligned} \tag{3.15}$$

The output of the inverse Fourier transform Eq. (3.15) is a complex matrix where either the real or imaginary part can be used to create ϕ_α. Here, the real part is used.

To simulate the "cross" terms of the CSDM, the cross-correlation of Eq. (3.15) must be computed. Making use of common trigonometric identities and Euler's formula, additional simplifications can be made to the resultant yielding

$$\begin{aligned} \langle \mathrm{Re}(\phi_x[i, j]) \, \mathrm{Re}(\phi_y[k, l]) \rangle = \sum_{m,n} \sigma_{\phi_x} \sigma_{\phi_y} \pi (\Gamma \ell_{\phi_x \phi_x} \ell_{\phi_y \phi_y}) \\ \exp\left\{ -\pi^2 \left(\frac{\ell^2_{\phi_x \phi_x} + \ell^2_{\phi_y \phi_y}}{2} \right) \left[\left(\frac{m}{N\Delta}\right)^2 + \left(\frac{n}{N\Delta}\right)^2 \right] \right\}. \\ \exp\left(\mathrm{j}\frac{2\pi}{N} m(i-k)\right) \exp\left(\mathrm{j}\frac{2\pi}{N} n(nj-l)\right) \frac{1}{(N\Delta)^2} \end{aligned} \tag{3.16}$$

By comparing the discrete function being transformed in Eq. (3.16) to the continuous cross-power spectral density function, i.e.,

$$\Phi_{\phi_x \phi_y}(f_x, f_y) = \sigma_{\phi_x} \sigma_{\phi_y} \pi \rho_{\phi_x \phi_y} \ell^2_{\phi_x \phi_y} \exp\left[-\pi^2 \ell^2_{\phi_x \phi_y} (f_x^2 + f_y^2) \right], \tag{3.17}$$

the following relationships are obtained:

$$\begin{aligned} \ell_{\phi_x\phi_y} &= \sqrt{\frac{\Gamma \ell_{\phi_x\phi_x}\ell_{\phi_y\phi_y}}{\rho_{\phi_x\phi_y}}} = \sqrt{\frac{\ell^2_{\phi_x\phi_x} + \ell^2_{\phi_y\phi_y}}{2}} \\ \Gamma &= \frac{\rho_{\phi_x\phi_y}\left(\ell^2_{\phi_x\phi_x} + \ell^2_{\phi_y\phi_y}\right)}{2\ell_{\phi_x\phi_x}\ell_{\phi_y\phi_y}} \\ \rho_{\phi_x\phi_y} &= \frac{2\Gamma \ell_{\phi_x\phi_x}\ell_{\phi_y\phi_y}}{\ell^2_{\phi_x\phi_x} + \ell^2_{\phi_y\phi_y}} \end{aligned} . \tag{3.18}$$

As demonstrated in further detail in Ref. [2], this method creates correlated random Gaussian phase screens necessary for the simulation and experimental generation of an EGSM source to control degrees of coherence and polarization.

3.3 Spatial Light Modulators

In this experiment, a dual SLM design serves as the active controller of the EGSM beam by means of displaying the random phase screens. From an understanding of the structure and operation of the SLM, potential sources of error can be identified. This section begins with descriptions of the relevant terminology, followed by discussions of how inherent design and manufacturing flaws are calibrated out.

3.3.1 Principles of Operation.

There are several different types of SLMs available for use, providing choices between transmissive and reflective SLMs, which may control either phase, amplitude, or both. SLMs have an expanding role in several optical areas where light control on a pixel-by-pixel basis is critical for optimum system performance. The SLMs chosen for this experiment are Boulder Nonlinear Systems (BNS) Model P512-0635 XY Series LC SLMs with a 512×512 pixel array and 15μm pitch, thus the focus of the following discussion will be based on electrically addressed phase-only nematic LC SLMs [3].

The structure of a liquid crystal on silicon (LCoS) SLM has several defining characteristics. SLMs control light based on a fixed spatial (pixel) pattern. The spacing between the centers of pixels in the pattern is referred to as pixel pitch. By design, polarized

light enters the device passing through a cover glass, transparent electrode, and LC layer. Beneath the LC layer are reflective aluminum pixel electrodes. The light reflects off this electrode layer and returns on the same path. A voltage induced electric field between the pixel electrode and the transparent electrode on the cover glass changes the optical properties of the LC layer. Because each pixel is independently controlled, a phase pattern may be generated by loading different voltages onto each pixel [3].

The chosen BNS SLMs are optimized to provide a full wave (2π rad) of phase stroke upon reflection at the λ = 635nm wavelength. These SLMs only provide phase modulation when the input light source is linearly polarized along the vertical axis. Additionally, the reflective pixel structure associated with a LCoS SLM backplane acts as an amplitude grating that diffracts some light into higher orders. In the experimental design, the SLMs are aligned to utilize reflected light off of the first diffraction order rather than the zeroth-order. An eight-step pixel grating is applied to the SLMs to direct energy into the first diffraction order. The rationale for this adjustment will be addressed in a later section.

3.3.2 Phase Response Calibration.

A SLM has a unique response in converting phase to digital command values. Several methods for calibrating phase response were considered, such as placing the SLM in a Michelson interferometer, double-slit aperture method, and using amplitude modulation [19]. A diffractive amplitude modulation method was chosen because, unlike in interferometry, the measurements are insensitive to vibrations.

To perform the amplitude modulation, the SLMs were aligned to use light reflected into the zeroth-order. The reflected light then passes through a lens after each SLM as shown in Fig. 3.1. An imaging sensor is placed at the respective focal plane of each lens. Prior to the light entering the detector, it passes through a quarter-wave plate (QWP) and linear polarizer (LP), which are required to collect the necessary irradiance to calculate the phase response. This method is thoroughly documented by Schmidt [19].

The SLMs interface with a controller providing 8-bits of pixel data. An array of commands is loaded into the SLM memory. Each command from 0 to 255 is a flat phase image, i.e., every addressable pixel in the array is set to the same value for each command. The LP prior to each SLM is aligned to 45-degrees, the QWP prior to the camera is aligned to 0-degrees, and the LP prior to the camera is aligned to 45-degrees for the first data collection. Each command is stepped through on each SLM and the irradiance on the sensor is measured. Using only this first measurement allows the phase to be computed over only half of the unit circle [19]. To complete the second measurement, the LP prior to the SLM remains aligned to 45-degrees, the QWP is then aligned to 45-degrees, and the LP remains aligned to 45-degrees. Each command is again stepped through on each SLM and the irradiance is measured. With the second measurement, phase can be measured over the entire unit circle, and a standard unwrapping technique can be used to compute the true physical phase commanded to the SLM [19].

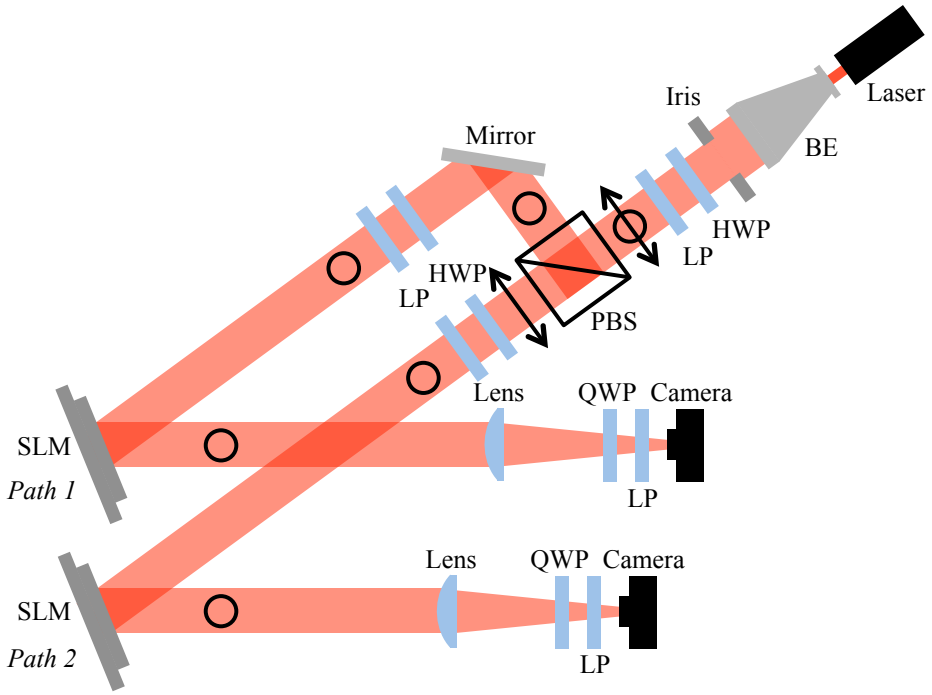

Figure 3.1: Schematic illustration of system setup for linear phase response calibration.

The irradiance measurements for each SLM with and without the QWP are plotted generating a power curve with maximums and minimums where each phase step is equal to π radians of phase, similar to Fig. 3.2(a) and Fig. 3.3(a). To obtain the phase, the irradiance data is input into a four-quadrant arctangent function

$$\phi_{\mathrm{SLM}} = \tan^{-1} \frac{\frac{1}{2} - I_2}{I_1 - \frac{1}{2}}, \tag{3.19}$$

where I_1 and I_2 are the irradiance data collected with the two measurements. This calculates phase that is wrapped over the interval $(-\pi, \pi]$. This wrapped phase can then be unwrapped [19]. A 2π region can then be selected to generate a look-up-table (LUT) which maps the desired phase command to the electrical command for each pixel.

During this calibration, difficulty was experienced generating power curves without saturation. The manufacturer provides linear phase response LUTs for each SLM. To verify the SLMs were working properly, the manufacturer LUTs were loaded to each SLM and the same procedure above was performed, stepping through each command. What would be expected if the LUTs were an accurate calibration would be a near linear unwrapped command to phase plot of a 2π region. As shown in Fig. 3.2(b) and Fig. 3.3(b), the manufacturer provided LUTs were adequate and used throughout this research effort.

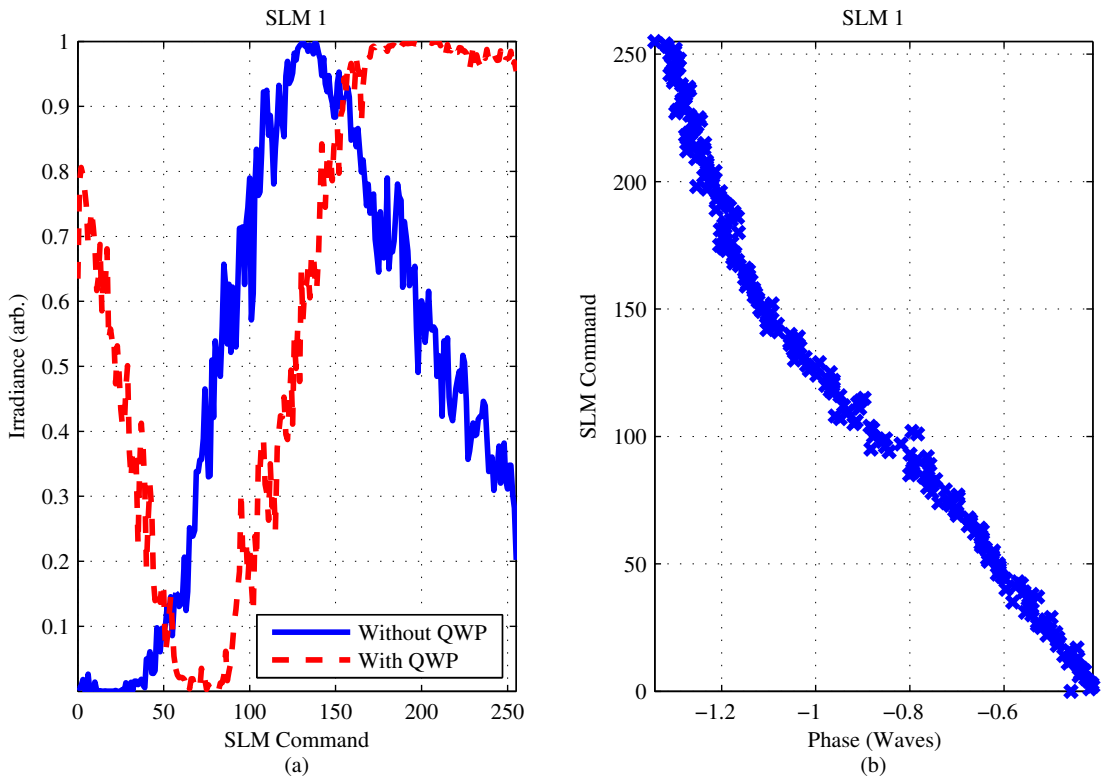

Figure 3.2: Linear phase response calibration plots for SLM 1 using manufacturer provided look-up-table showing (a) measured irradiance with and without a quarter-wave plate and (b) the unwrapped phase.

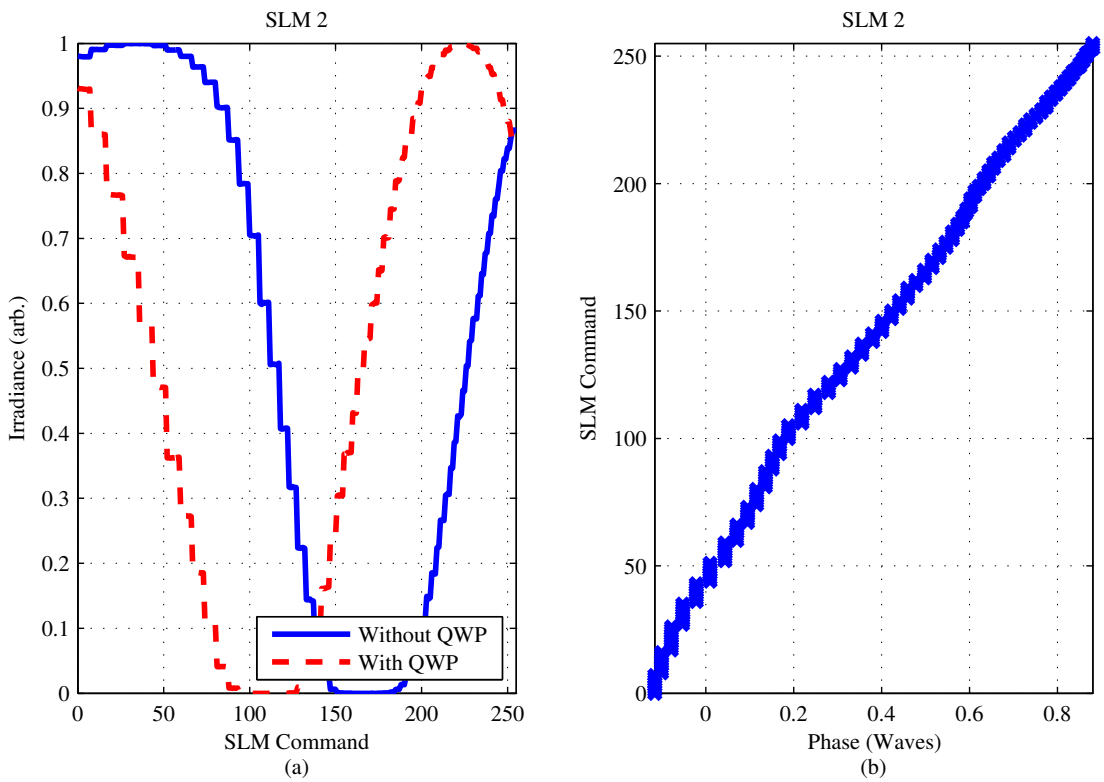

Figure 3.3: Linear phase response calibration plots for SLM 2 using manufacturer provided look-up-table showing (a) measured irradiance with and without a quarter-wave plate and (b) the unwrapped phase.

To smooth the curves and optimize the speed of converting phase to commands, a Padé fit is applied to the LUT data for each SLM as shown in Fig. 3.4. A Padé function, $P(x)$, has the form

$$P(x) = \frac{\sum_{m=0}^{M} a_m x^m}{1 + \sum_{n=0}^{N} a_n x^n}, \tag{3.20}$$

where where P is the dependent variable, x is the independent variable, m and n are integer indices, M and N are the highest polynomial orders in the numerator and denominator, respectively, and where a_m and b_n are the polynomial coefficients in the numerator and denominator, respectively.

To use this calibration for commanding phases onto the SLM, phase values (one value for each pixel) on the interval $[0, 2\pi)$ are sent to the SLM and converted directly to an array of command values using a Padé function with the appropriate coefficients rather than searching a LUT [19]. This greatly improves the performance and efficiency of the SLM control code.

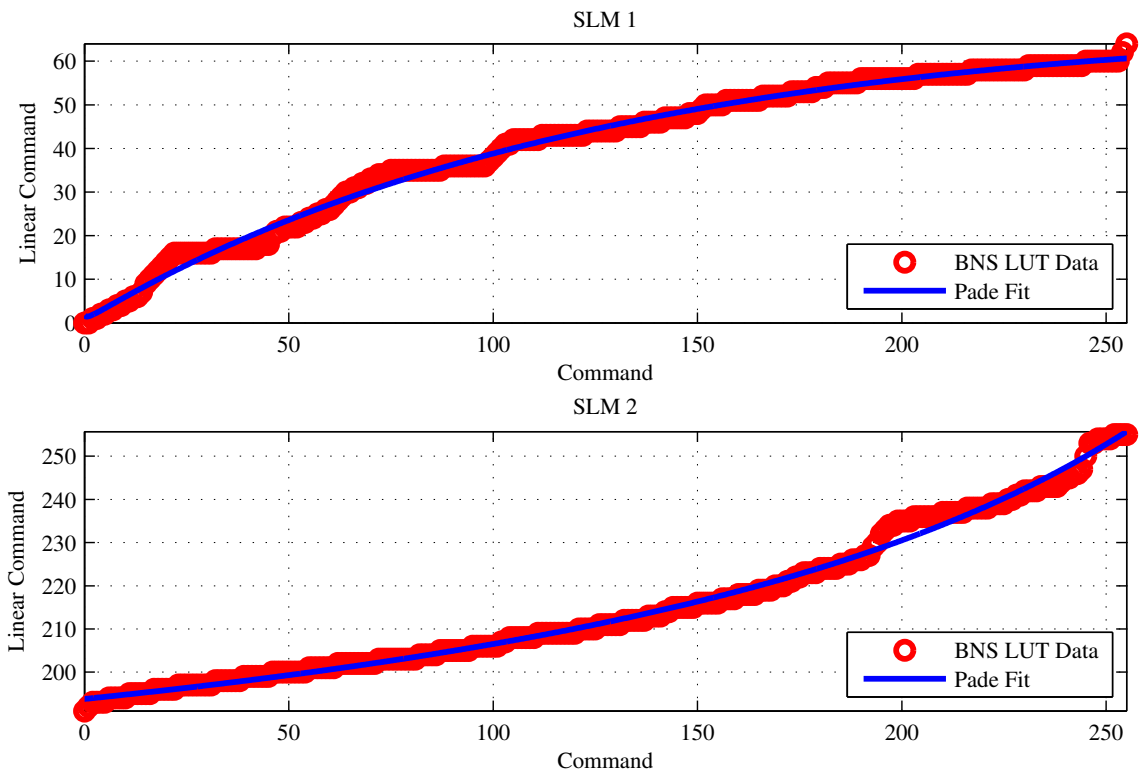

Figure 3.4: Pade fit to manufacturer provided look-up-table data for SLM 1 and SLM 2.

3.3.3 Static Aberration Calibration.

A LCoS SLM has an inherent static aberration across its full aperture due to the manufacturing process [19]. Thus, the shape of this aberration must be measured to apply the appropriate phase map to the SLM to compensate. There are many different methods to perform a static aberration calibration.

Parametric optimization was the first method considered but was prohibited by the requirement to capture an image in both the lens plane and focal plane. The SLM aperture is too large to fully fit on the sensor array and it was not possible to demagnify the SLM aperture given the testbed and limited amount of space. The next calibration method considered used interferometry, which provides a direct measurement of the SLMs inherent phase distortion. The measurement comes from interferogram analysis using a Michelson interferometer setup. This method was attempted with little success. An interferogram was somewhat visible but this method was ultimately too sensitive to vibrations.

The last method considered and chosen was an iterative Fourier transform method, using forward and inverse Fourier transforms to propagate a field back and fourth between the pupil and focal planes while imposing physical constraints at both planes. This approach to phase retrieval is known as the Gerchberg-Saxton algorithm [10].

The Gerchberg-Saxton algorithm is an error-reduction algorithm, as the error in the solution decreases with every iteration [10]. Convergence occurs when the decrease in error stagnates. Phase diversity is used here to extend the original Gerchberg-Saxton algorithm [10]. Figure 3.5 is a flow chart showing the modified algorithm with phase diversity. Stepping through the chart, an initial guess for the static aberration is made. The phase function is multiplied by the pupil function. Then, a known phase aberration is added to the static phase estimate. Next, a Fourier transform translates the pupil field to the focal plane. Here the calculated amplitude is substituted by the measured amplitude from the known phase aberration. An inverse Fourier transform then translates the modified field to the pupil plane where the applied known aberration is subtracted from the resulting phase. This constitutes one iteration; the remaining phase is an estimate for both the pupil amplitude and static aberration [10]. Each successive iteration through this loop ideally uses a new pair of known pupil phase and measured focal plane amplitudes with the static phase aberration estimates improving each time. For practicality, the known phase

aberrations and captured amplitudes are a finite set of measurements and the algorithm loops through them until a stopping criterion is met. What remains when the algorithm stops is the static aberration phase estimate.

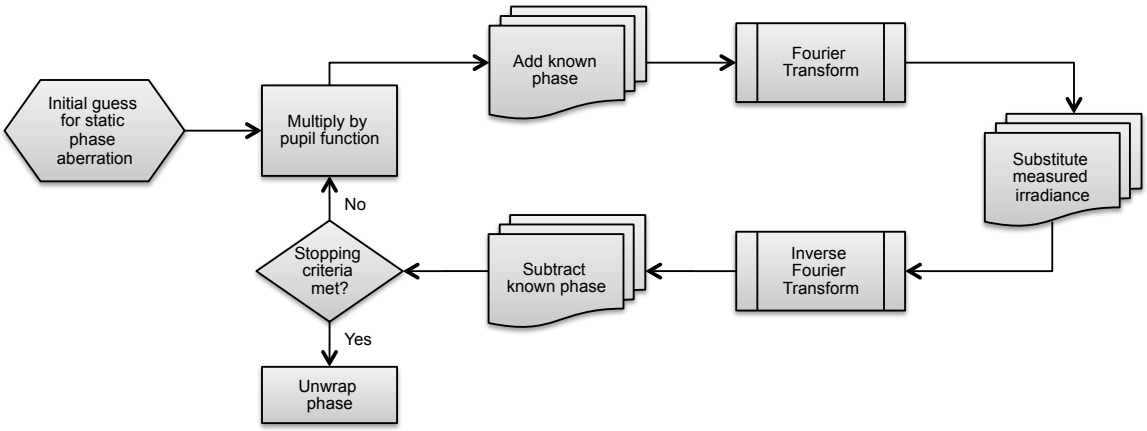

Figure 3.5: Modified Gerchberg-Saxton algorithm flow chart for iterative Fourier transform calibration method.

After successfully verifying the algorithm in simulation using Zernike polynomials, the algorithm was ready to be used to calibrate the SLMs. The experimental procedure first required the generation of unique phase screens to be applied to each SLM. To provide phase diversity, Zernike terms 3-9 were used to make three sets of phase screens with varying peak aberration coefficients, totaling 21 phase screens. These screens were commanded to each SLM and the corresponding diffraction patterns were gathered at the focal plane. The known phase screens and corresponding collected images were then loaded into the iterative Fourier transform algorithm to loop through the images as described above with a set maximum of 300 iterations or until a sum-squared-error threshold was reached. Each SLM was calibrated individually as shown in Figs. 3.6 and 3.7.

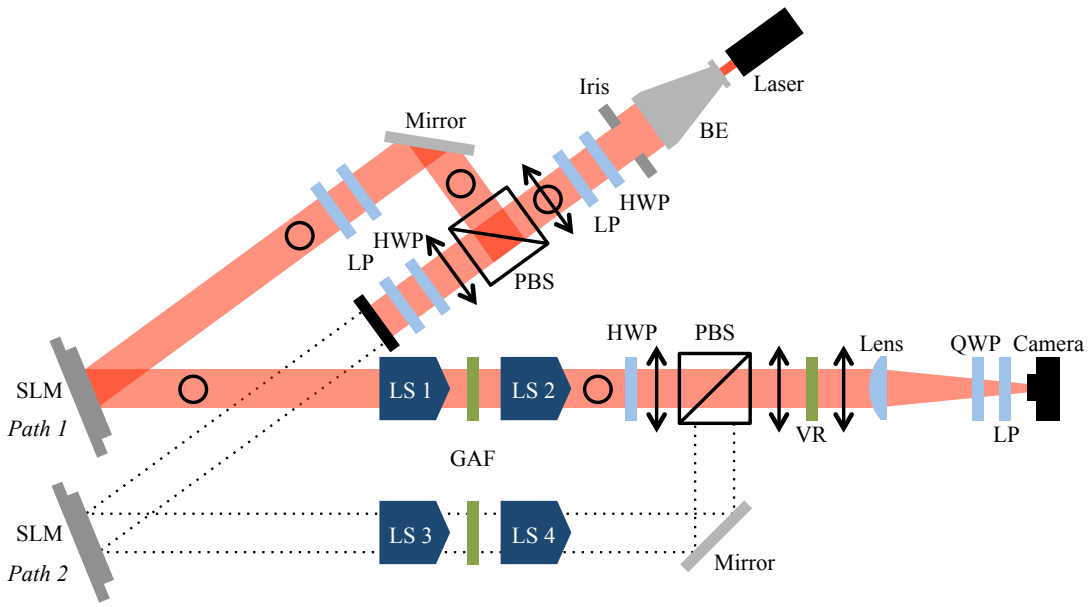

Figure 3.6: Schematic illustration of system setup for static phase aberration calibration for Path 1.

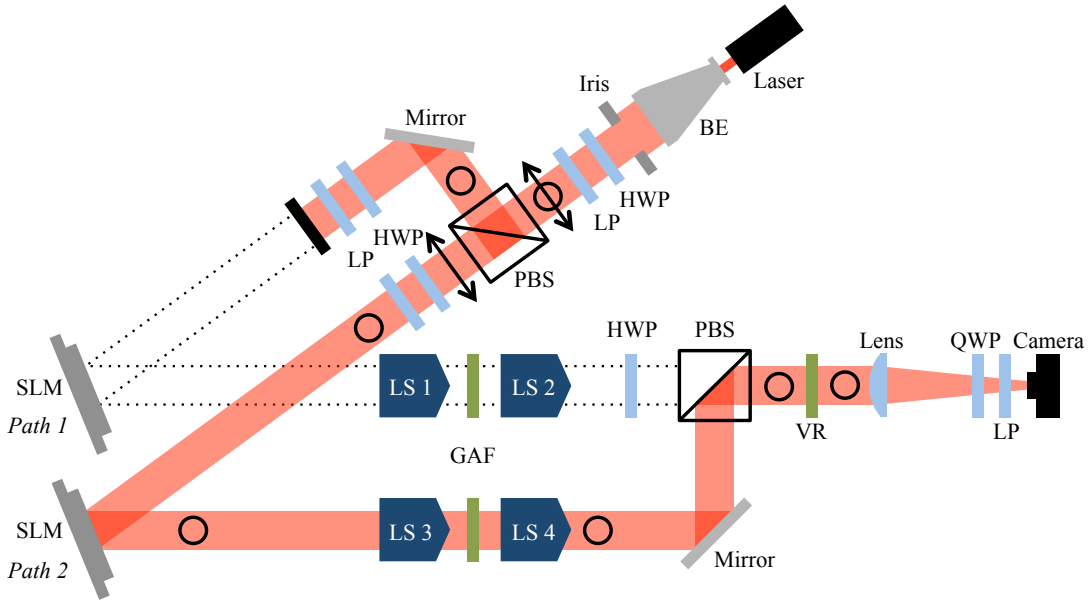

Figure 3.7: Schematic illustration of system setup for static phase aberration calibration for Path 2.

3.3.4 Comparison of Results.

The intention of performing both the linear phase response and the static aberration calibrations is to flatten the wavefront at the pupil plane, leaving only the effect of diffraction by the pupil itself. The square aperture of the SLM is the pupil, the far-field diffraction pattern is expected to be a 2-D sinc pattern. The static aberration estimates gathered from the above method for each SLM are shown in Fig. 3.8. The observed diffraction pattern for each SLM are shown without correction in Figs. 3.9(a) and 3.10(a) and with correction in Figs. 3.9(b) and 3.10(b).

When performing the static aberration calibration, the initial alignment of the SLMs used the light reflected into the zeroth-order as described in the linear phase response calibration. The static calibration was repeatedly failing to provide a good aberration estimate. It was eventually discovered there was a specular reflection off the front face of SLM glass that was not being controlled by the SLMs. This reflection traveled the same optical path to the sensor and was placing a bright spot in the amplitude measurements for which the algorithm could not account. To correct this issue, the alignment of the SLMs was adjusted to use the light reflected into the first-order as stated above. This adjustment was not made for the linear phase response calibration and it is unknown if this anomaly affected those calibration results.

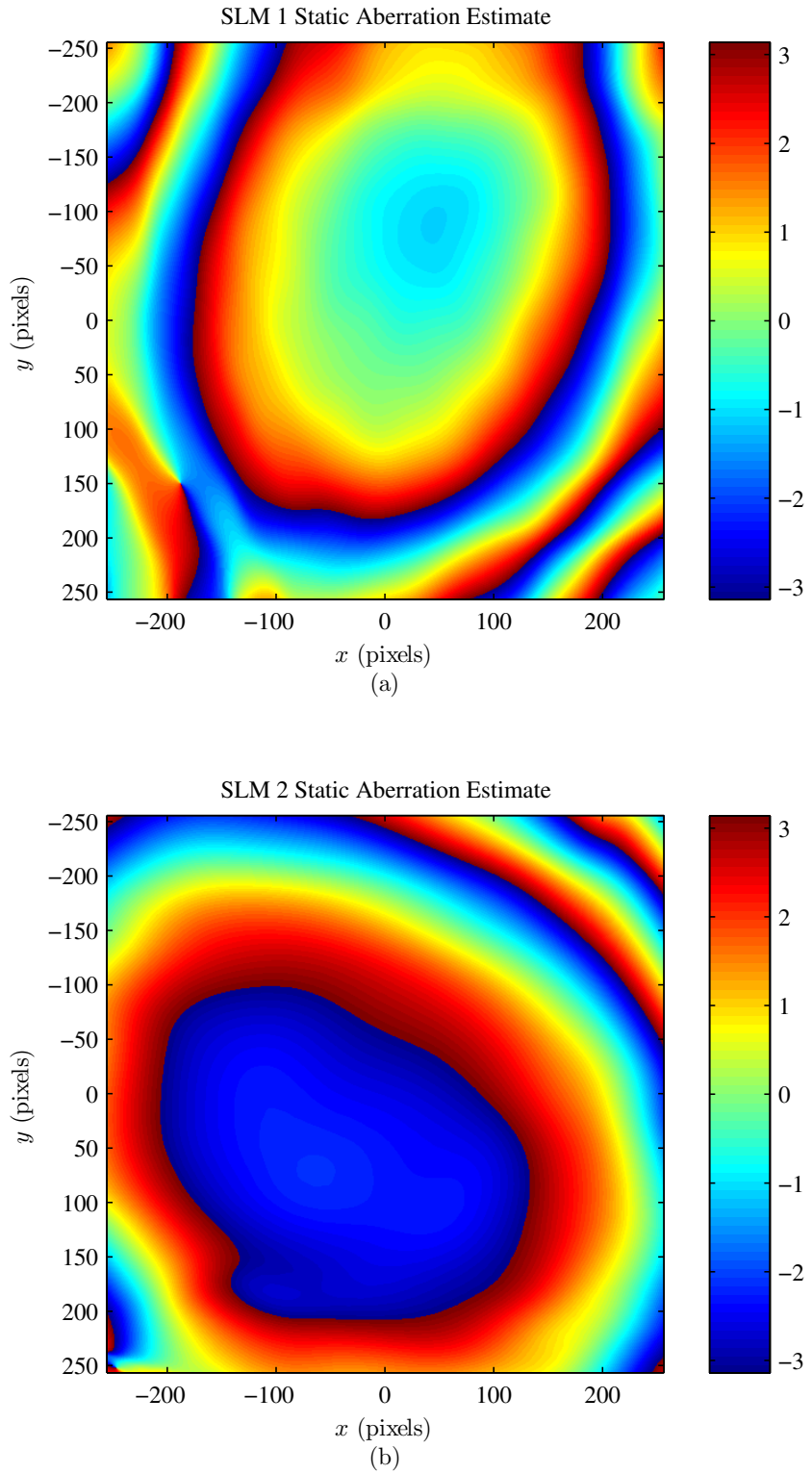

Figure 3.8: Static phase aberration estimates for (a) SLM 1 and (b) SLM 2.

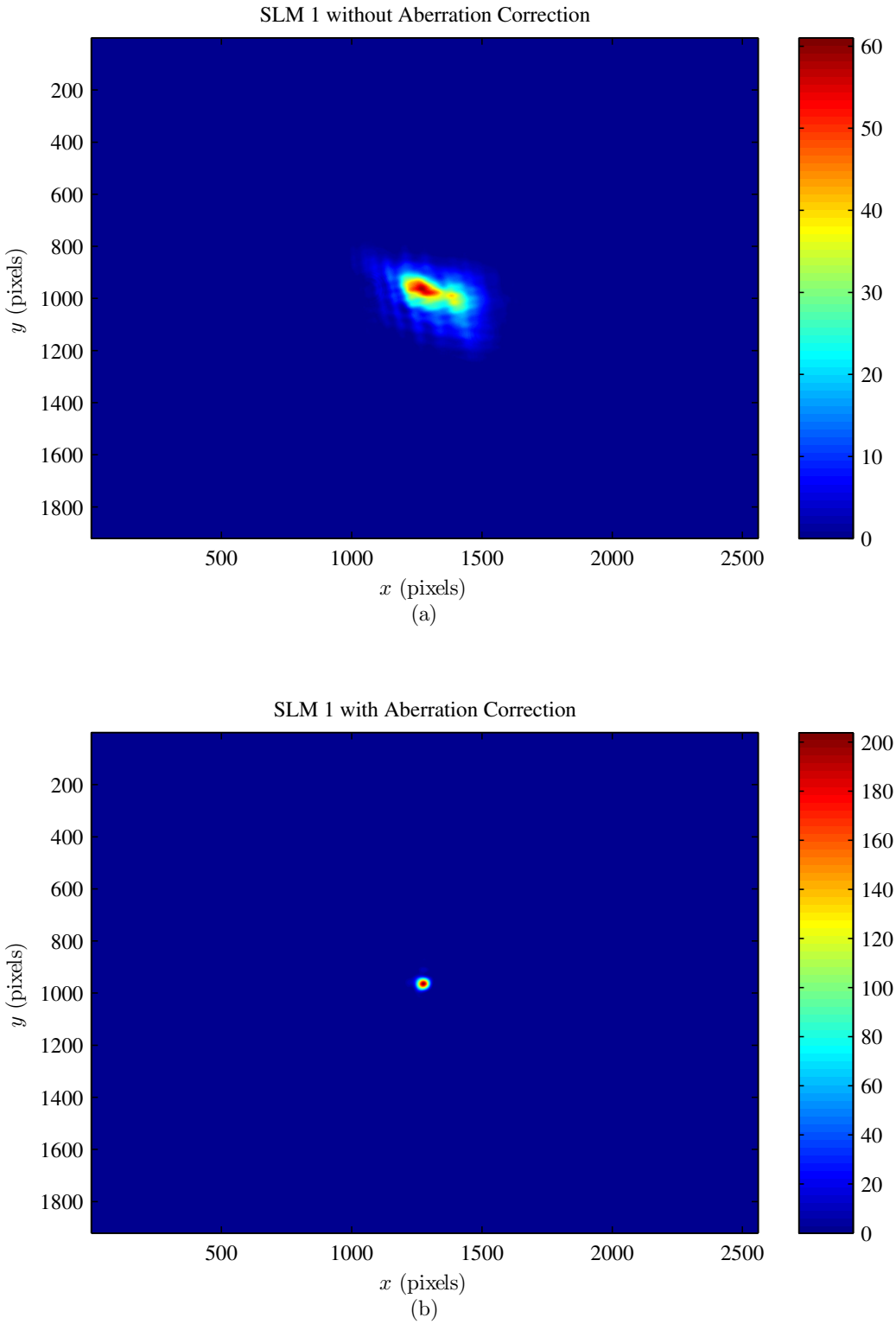

Figure 3.9: Static aberration calibration diffraction patterns showing a flat phase applied to SLM 1 and propagated through the system to the observation plane (a) without correction applied for the static aberration and (b) with correction applied for the static aberration.

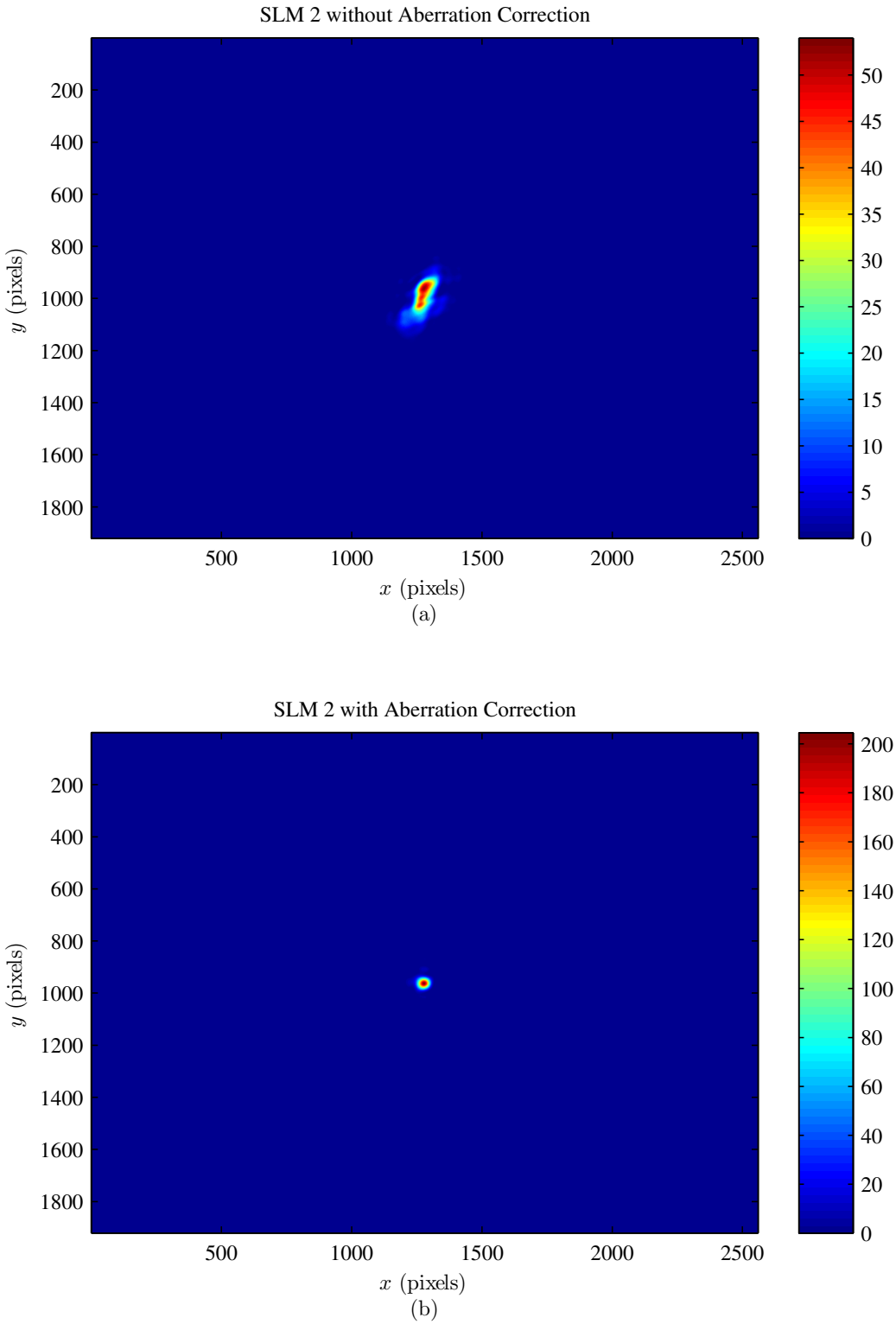

Figure 3.10: Static aberration calibration diffraction patterns showing a flat phase applied to SLM 2 and propagated through the system to the observation plane (a) without correction applied for the static aberration and (b) with correction applied for the static aberration.

3.4 System Model

3.4.1 Design.

For the experiment designed for this research, the source chosen to generate the EGSM beam is a HeNe gas laser, whose radiation is almost completely coherent and completely polarized, with an output wavelength of $\lambda = 632.8$nm. As shown in Fig. 3.11, the beam from the laser source passes through a beam expander. After leaving the beam expander, the expanded beam passes through an iris. The beam expander is adjusted to fill a minimum region of interest while also maintaining collimation. This was tested after each optical element discussed below. The iris was adjusted to prevent the beam from over-filling the optical elements while still filling the region of interest.

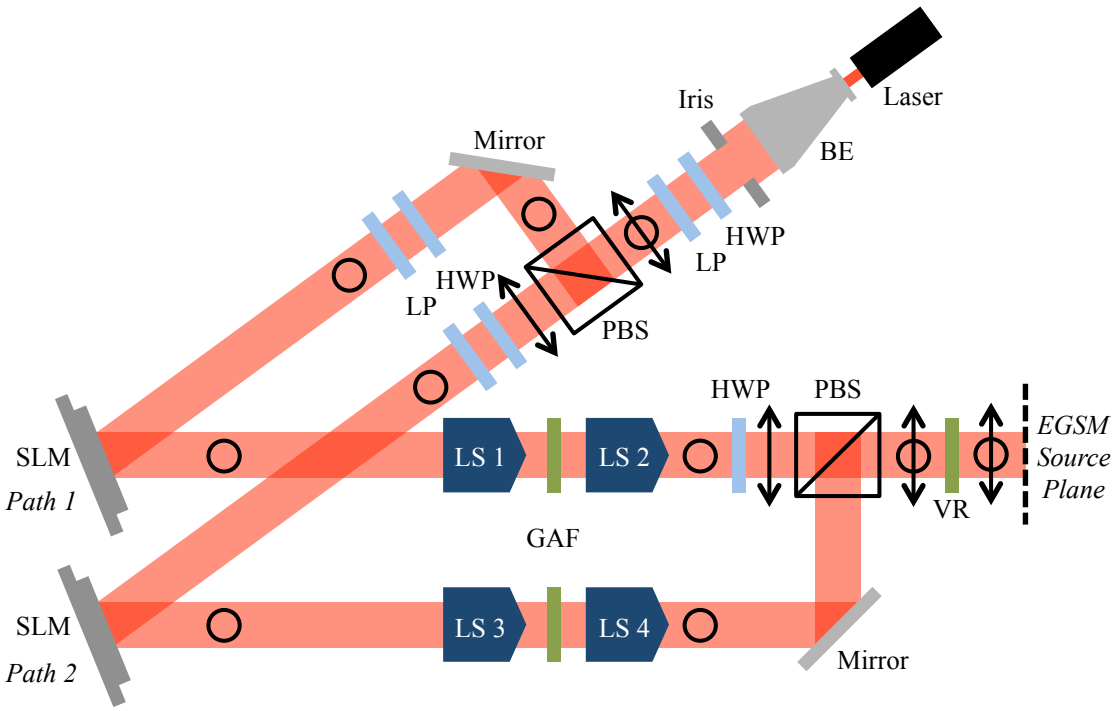

Figure 3.11: Schematic illustration of experiment design to generate an EGSM source.

After the iris, the beam passes through a half-wave plate (HWP) and LP. The purpose of these optical elements is to control the amplitude of the beam. Following these elements, the beam enters a polarizing beam splitter (PBS). The PBS allows the horizontally polarized light to pass through and reflects the vertically polarized light. These beam components constitute the *Path 1* (horizontally polarized axis) and *Path 2* (vertically polarized axis), as referenced from this point forward and labeled in Fig. 3.11.

As previously discussed in Section 3.4, the SLMs used in this experiment act only on vertically polarized light. The portion of the beam passing through the PBS is horizontally polarized. After leaving the PBS, this component passes through another HWP and LP. The HWP is used to control the relative amplitude (A_y) of *Path 2* of the EGSM beam. The LP is used to ensure only vertically polarized light is incident on the SLM. The portion of the beam reflected by the PBS is vertically polarized. After leaving the PBS, this component also passes through another HWP and LP. Again, the HWP is used to control the relative amplitude (A_x) of *Path 1* of the EGSM beam. The LP is used to ensure only vertically polarized light is incident on the SLM.

Both beam components are now incident on the LC SLMs. The SLMs display the correlated Gaussian random phase screens. The SLMs are placed and oriented to reflect the beams parallel to each other, with a grating applied to direct the beam energy into the first-order.

Following the SLM on *Path 1* is a 4-*f* lens system (LS1) shown in Fig. 3.12 which serves multiple purposes. This lens system has an iris at the focal plane between the lenses. Both lenses used are plano-convex and have a 350mm focal length so as to not magnify or demagnify the beam. The first purpose of the lens system is to remove unwanted diffraction orders with the iris. If the diffraction orders were allowed to enter the optical path, the experimental results would be negatively affected. No calculation was performed

to identify the diffraction limited spot size present in the focal plane where the iris is positioned; the iris was adjusted visually.

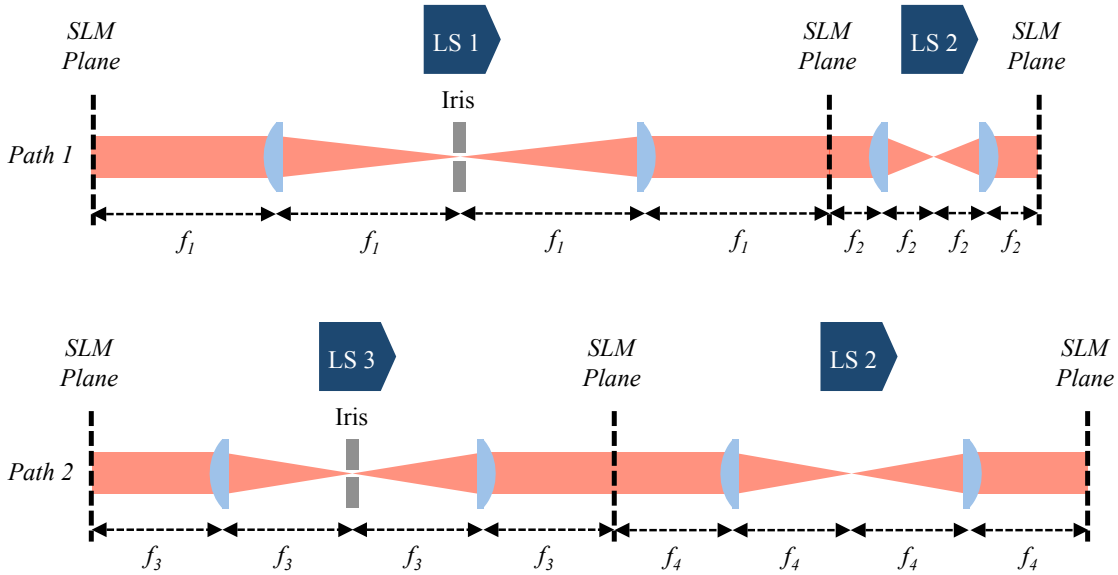

Figure 3.12: Exploded view of lens systems on Path 1 and Path 2 of the experiment design highlighting the translated SLM planes and lens focal lengths.

The second purpose of this 4-*f* lens system is to translate the SLM plane. This plane is located at the focal plane of the second lens in the system. This plane translation is necessary to prevent the addition of phase curvature. The 4mm Gaussian amplitude filter (GAF) is placed at this point.

Following the GAF on *Path 1* is a second 4-*f* lens system (LS2) shown in Fig. 3.12 which serves the purpose of translating the SLM plane again for the placement of the LC variable retarder (VR). The lenses used are plano-convex and have a 100mm focal length. Prior to the VR, there are several other optical elements requiring discussion. A HWP is placed within the lens system to transform the vertically polarized beam to horizontal

polarization. After the now horizontally polarized beam leaves the second lens in the system, it passes through another PBS for recombination.

Following the SLM on *Path 2* is a 4-*f* lens system (LS3) shown in Fig. 3.12 which again serves the same purposes as the first 4-*f* system on *Path 1*. This lens system also has an iris at the focal plane between the lenses. The lenses used are plano-convex with a 250mm focal length. The iris again is used to remove unwanted diffraction orders. At the focal plane of the second lens in the system (the translated SLM plane) is a 3mm GAF.

Following the GAF on *Path 2* is a second 4-*f* lens system (LS4) shown in Fig. 3.12 which translates the SLM plane again for placement of the previously mentioned VR. The lenses used are plano-convex with a 225mm focal length. After the vertically polarized beam passes through the second lens in the system, it reflects through the PBS previously mentioned for recombination.

The PBS at the end of path recombines the *Path 1* and *Path 2* beam components. The final element the recombined beam must pass through is the VR, placed in the translated SLM plane. The ThorLabs LCC1223-A full-wave LC VR is electrically controlled by a ThorLabs LCC25 LC controller. In order to only control the phase of the incident EGSM beam, the linearly polarized input beam must have a polarization axis aligned with the optical axis of the VR [22]. As the voltage, V_{rms}, is increased on the controller, the phase offset in the beam is decreased. The VR is oriented to retard the horizontally polarized axis, i.e., alter the optical path length of *Path 1* with respect to *Path 2* and provide $\angle B_{xy}$. Note the VR was not calibrated due to time constraints and was set to minimize the amount of retardance applied for purposes of this experiment.

The beam exiting the VR constitutes an instantaneous realization of an EGSM beam at the source plane. Immediately after the VR is a 1000mm focal length plano-convex lens. The purpose of this lens is to focus the beam to the sensor. The reason this lens is required is due to fact that the sensor is smaller than the SLM. Given the constraints on the table

size, there was not room to feasibly include an additional 4-f lens systems to demagnify the beam prior to the sensor. For this reason, the experiment measures the EGSM observation plane rather than the source plane.

3.4.2 Polarization Analyzer.

To collect the desired data from the generated EGSM source, the beam was passed through the previously mentioned focusing lens to a quarter-wave plate and linear polarizer. These two elements constitute what is referred to as a polarization state analyzer. Following this analyzer is the detector, placed at the focal plane of the 1000mm focusing lens. This focal plane is the EGSM observation plane.

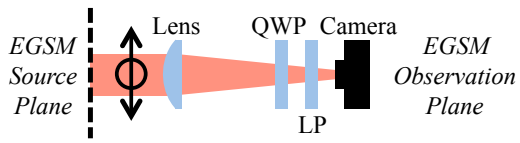

Figure 3.13: Schematic illustration of polarization state analyzer composed of a focusing lens, quarter-wave plate, linear polarizer, and imaging camera.

The detector used is a Edmund Optics 5012M CMOS imaging sensor with a 2560×1920 pixel resolution and pitch of 2.2μm [5]. The region of interest for purposes of this experiment was cropped to 1024×1024 to reduce the amount of data stored in the collected files. The images were able to be cropped due to the fact that light incident on the sensor was not scattered outside the chosen region. Additionally, the detector was not calibrated, which could lead to possible errors in the gathered data.

3.4.3 Data Collected.

With this experimental design, the desired measurements at the EGSM observation plane are the Stokes parameters, DoP, and SDoC. None of these measurements are directly available from the imaging sensor so these results must be computed from the

irradiance incident on the sensor. With the help of the previously mentioned polarization state analyzer, the QWP and LP are set to specific orientations as detailed in Tab. 3.1. The irradiance images gathered for each set of orientations allows the unnormalized Stokes parameters to be calculated as [20]

$$\begin{aligned} S_0 &= I_H + I_V \\ S_1 &= I_H - I_V \\ S_2 &= I_{+45} - I_{-45} \\ S_3 &= I_R - I_L \end{aligned}, \tag{3.21}$$

where S_0 is the incident irradiance, S_1 is the horizontally polarized irradiance I_H minus the vertically polarized irradiance I_V, S_2 is the 45-deg polarized irradiance I_{+45} minus the 135-deg polarized irradiance I_{-45}, and S_3 is the right-hand circularly polarized irradiance I_R minus the left-hand circularly polarized irradiance I_L. The wave plate and polarizer orientations required to collect these irradiance components are defined in Tab. 3.1.

Table 3.1: Polarization Analyzer Orientations

Irradiance	**QWP**	**LP**
I_H	0-deg	0-deg
I_V	90-deg	90-deg
I_{+45}	45-deg	45-deg
I_{-45}	-45-deg	-45-deg
I_R	-45-deg	0-deg
I_L	45-deg	0-deg

With the Stokes parameters defined and calculated, the DoP for the total beam is then calculated as

$$\text{DoP} = \frac{\sqrt{S_1^2 + S_2^2 + S_3^2}}{S_0} \tag{3.22}$$

and the degree of linear polarization (DoLP) is calculated as

$$\text{DoLP} = \frac{\sqrt{S_1^2 + S_2^2}}{S_0}, \tag{3.23}$$

which, if $S_3 \approx 0$, as is the case in some of the experimental results, DoP $\approx$ DoLP.

The last desired measurement is the SDoC. This is not directly measurable nor able to be calculated using the gathered irradiance images because an electric field would have to be captured by the detector. Given the degree of coherence (DoC) of each CSDM element as defined by

$$\mu_{\alpha\beta} = \frac{W_{\alpha\beta}(\boldsymbol{\rho}_1, \boldsymbol{\rho}_2)}{\sqrt{W_{\alpha\beta}(\boldsymbol{\rho}_1, \boldsymbol{\rho}_1) W_{\alpha\beta}(\boldsymbol{\rho}_2, \boldsymbol{\rho}_2)}} \qquad \begin{pmatrix} \alpha = x, y \\ \beta = x, y \end{pmatrix}, \tag{3.24}$$

a comparable measurement needs to be taken to obtain this quantity. Thus, taking the square of the modulus yields

$$|\mu_{\alpha\beta}|^2 = \frac{W_{\alpha\beta}(\boldsymbol{\rho}_1, \boldsymbol{\rho}_2) W^*_{\alpha\beta}(\boldsymbol{\rho}_1, \boldsymbol{\rho}_2)}{S_\alpha(\boldsymbol{\rho}_1) S_\beta(\boldsymbol{\rho}_2)} \qquad \begin{pmatrix} \alpha = x, y \\ \beta = x, y \end{pmatrix}. \tag{3.25}$$

Using the gathered irradiance images as compared to the electric fields and applying the Gaussian Moment Theorem yields

$$\begin{aligned} \langle I_\alpha(\boldsymbol{\rho}_1) I_\beta(\boldsymbol{\rho}_2) \rangle =& \langle E^*_\alpha(\boldsymbol{\rho}_1) E^*_\beta(\boldsymbol{\rho}_2) E_\alpha(\boldsymbol{\rho}_1) E_\beta(\boldsymbol{\rho}_2) \rangle \\ =& \langle E^*_\alpha(\boldsymbol{\rho}_1) E_\alpha(\boldsymbol{\rho}_1) \rangle \langle E^*_\beta(\boldsymbol{\rho}_2) E_\beta(\boldsymbol{\rho}_2) \rangle + \langle E^*_\alpha(\boldsymbol{\rho}_1) E_\beta(\boldsymbol{\rho}_2) \rangle \langle E^*_\beta(\boldsymbol{\rho}_2) E_\alpha(\boldsymbol{\rho}_1) \rangle \\ =& S_\alpha(\boldsymbol{\rho}_1) S_\beta(\boldsymbol{\rho}_2) + W_{\alpha\beta}(\boldsymbol{\rho}_1, \boldsymbol{\rho}_2) W^*_{\alpha\beta}(\boldsymbol{\rho}_1, \boldsymbol{\rho}_2) \\ & (\alpha = x, y \text{ and } \beta = x, y) \end{aligned} . \tag{3.26}$$

This simplifies to

$$|\mu_{\alpha\beta}|^2 = \frac{\langle I_\alpha(\boldsymbol{\rho}_1) I_\beta(\boldsymbol{\rho}_2) \rangle}{S_\alpha(\boldsymbol{\rho}_1) S_\beta(\boldsymbol{\rho}_2)} - 1 \qquad \begin{pmatrix} \alpha = x, y \\ \beta = x, y \end{pmatrix}, \tag{3.27}$$

which is the normalized fourth-order correlation function (FOCF) expanded in terms of the DoC [4, 23].

For the purposes of providing a cleaner result when comparing the gathered experimental data to the simulated and theoretical data, this relationship is then rearranged as

$$\langle I_\alpha(\boldsymbol{\rho}_1) I_\beta(\boldsymbol{\rho}_2)\rangle = W_{\alpha\beta}(\boldsymbol{\rho}_1, \boldsymbol{\rho}_2) W^*_{\alpha\beta}(\boldsymbol{\rho}_1, \boldsymbol{\rho}_2) + S_\alpha(\boldsymbol{\rho}_1) S_\beta(\boldsymbol{\rho}_2) \qquad \begin{pmatrix} \alpha = x, y \\ \beta = x, y \end{pmatrix}, \tag{3.28}$$

where the irradiance correlation function on the left side of the equation is readily available from the experimentally gathered irradiance images and the values in the sum on the right side of the equation are readily available from the simulated and theoretical data.

IV. Analysis and Results

Chapter 4 presents the results of two different EGSM source generation experiments. The first (Experiment I) was an elliptically partially polarized EGSM source with a fully-populated CSDM. The second (Experiment II) was a linearly, partially polarized EGSM source with the off-diagonal elements of the CSDM equal to zero. Table 4.1 details the desired and actual EGSM source parameters used in Experiment I and II. Table 4.2 details the required phase screen values. The relations between the desired EGSM source and phase screen parameters forms a system of coupled nonlinear equations which can not be analytically inverted [2]. To determine the phase screen parameters from the desired source parameters, constrained nonlinear optimization was used to find the optimal parameters. For simulation and theory, 512 points per side and a spacing of 15μm were used to discretize the fields along *Paths 1* and *2* in Fig. 3.11. These numbers were chosen to match the BNS Model P512-0635 SLM. A wavelength of λ = 632.8nm was assumed. The results for Experiment I and II are detailed in following sections.

Table 4.1: EGSM Source Parameters

Experiment I			**Experiment II**		
Parameter	***Desired***	***Actual***	***Parameter***	***Desired***	***Actual***
A_x	1.3	1.3	A_x	1.3	1.3
A_y	1	1	A_y	1	1
$\angle B_{xy}$	0	0	$\angle B_{xy}$	0	0
σ_x (mm)	2.8	2.8	σ_x (mm)	2.8	2.8
σ_y (mm)	2.1	2.1	σ_y (mm)	2.1	2.1
δ_{xx} (mm)	0.40406	0.42643	δ_{xx} (mm)	0.40406	0.40406
δ_{yy} (mm)	0.30305	0.30972	δ_{yy} (mm)	0.30305	0.30305
δ_{xy} (mm)	0.44447	0.41705	δ_{xy} (mm)	0.44447	0.44447
$\lvert B_{xy}\rvert$	0.15	0.14942	$\lvert B_{xy}\rvert$	0	2.5513e-6

Table 4.2: EGSM Phase Screen Parameters

Experiment I		**Experiment II**	
Parameter	***Value***	***Parameter***	***Value***
$\ell_{\phi_x\phi_x}$ (mm)	2.4	$\ell_{\phi_x\phi_x}$ (mm)	2.9
$\ell_{\phi_y\phi_y}$ (mm)	1.4	$\ell_{\phi_y\phi_y}$ (mm)	1.7
σ_{ϕ_x}	3.9143	σ_{ϕ_x}	5.0552
σ_{ϕ_y}	3.1416	σ_{ϕ_y}	6.3124
Γ	1	Γ	0.6225

4.1 Experiment I Results

Experiment I was completed using 10,000 realizations to generate the EGSM source. Figure 4.1 shows the experimental results for the normalized Stokes parameters compared to the results of 10,000 simulations and theory. The images are organized such that the theoretical, simulation, and experimental results are along the columns—theoretical results are Figs. 4.1(a), 4.1(d), 4.1(g), and 4.1(j); simulation results are Figs. 4.1(b), 4.1(e), 4.1(h), and 4.1(k); experimental results are Figs. 4.1(c), 4.1(f), 4.1(i), and 4.1(l). Each row of images in Fig. 4.1 is a Stokes parameter—S_0 are Figs. 4.1(a), 4.1(b), and 4.1(c); S_1 are Figs. 4.1(d), 4.1(e), and 4.1(f); S_2 are Figs. 4.1(g), 4.1(h), and 4.1(i); S_3 are Figs. 4.1(j), 4.1(k), and 4.1(l). Figure 4.2 shows slices of the Stokes parameters for additional visualization of the results. The plots are organized such that the theoretical, simulation, and experimental curves overlay each other for each Stokes parameter—S_0 is Fig. 4.2(a), S_1 is Fig. 4.2(b), S_2 is Fig. 4.2(c), and S_3 is Fig. 4.2(d).

Overall the experimental Stokes parameters in Fig. 4.1 match the shape of the simulated and theoretical parameters well, showing good agreement. Noticeable with the experimental results for S_1 and S_2 in Figs. 4.1(f) and 4.1(i) is an apparent shift of the absolute value of the maxima at the center of the beam. This is due to spatial registration issues. Because the Stokes parameters (other than S_0) involve difference when calculating using the experimental data, any misregistration artifacts are amplified [20]. The misregistration visible in these parameters is a result of the rotating polarizers used to capture the different polarized irradiance components.

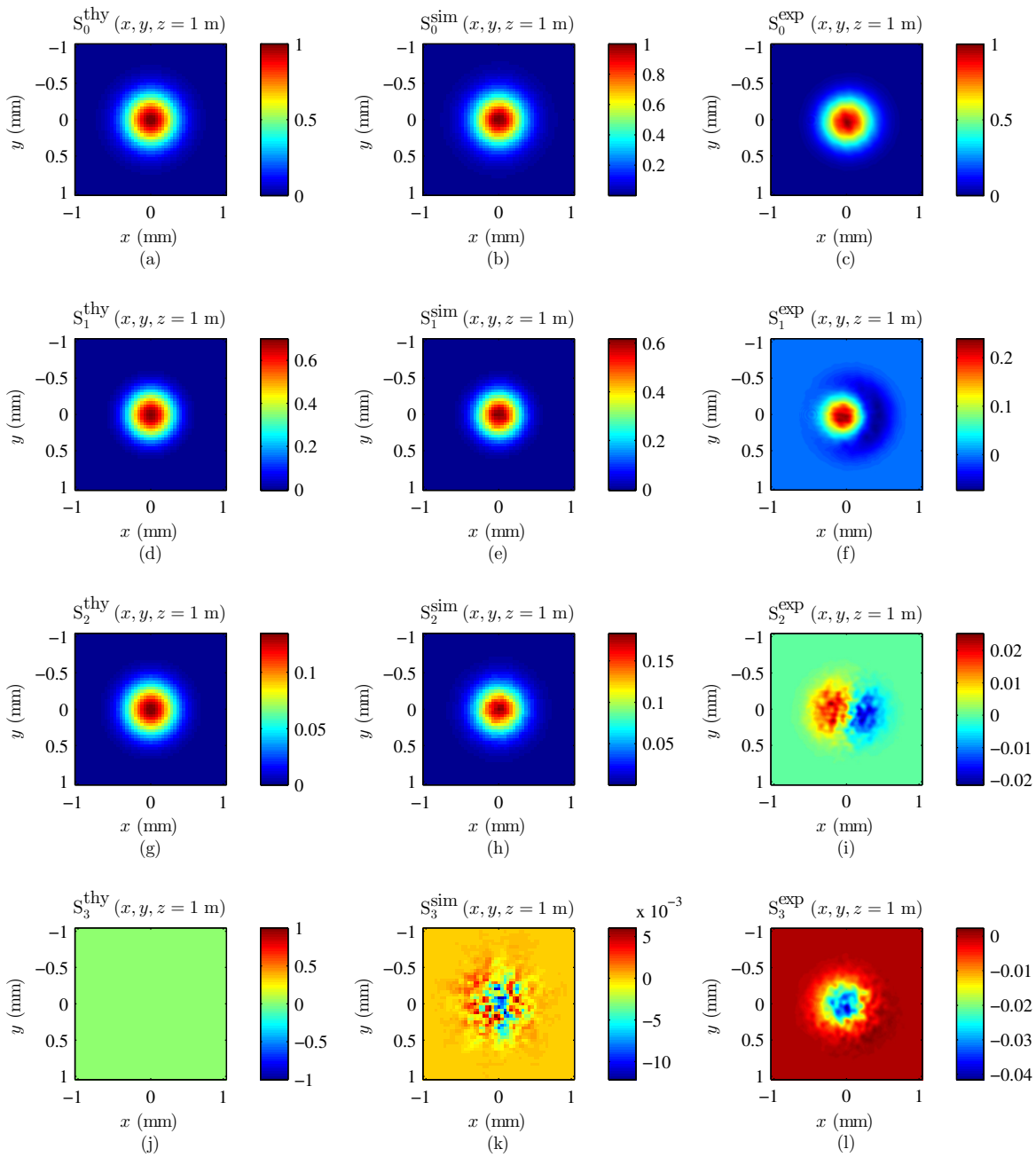

Figure 4.1: Experiment I Stokes parameter results compared with simulation and theory. The rows are S_0, S_1, S_2, and S_3, respectively, while the columns are the theory, simulation, and experimental results, respectively.

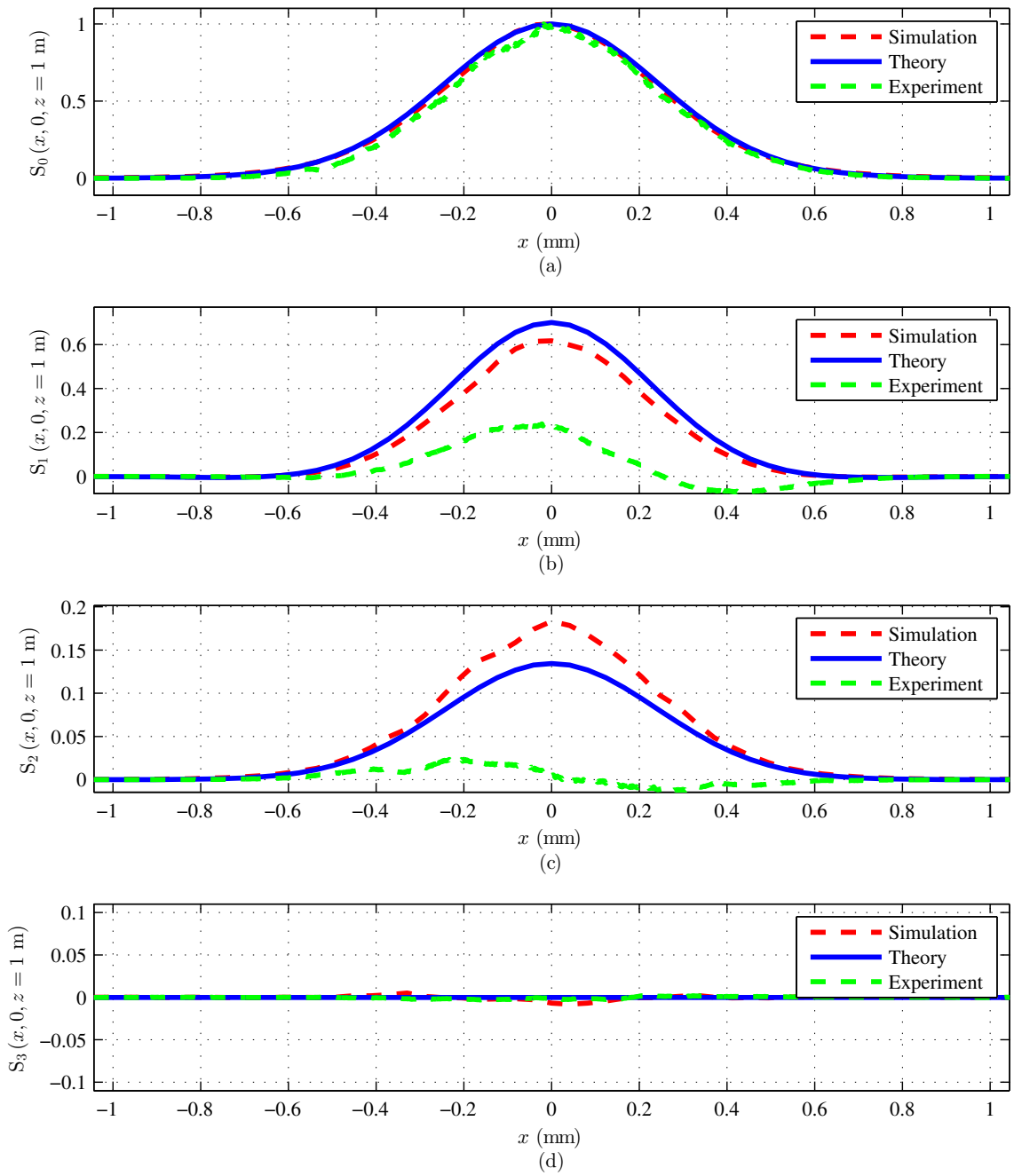

Figure 4.2: Experiment I Stokes parameter results compared with simulation and theory. The theory, simulation, and experiment slices plotted together for each of (a) S_0, (b) S_1, (c) S_2, and (d) S_3.

Further, the simulation and theoretical results visible in Fig. 4.2 do not match as well as published results [2]. This is due to the fact that the SLM is cropping the beam prior to passing through the GAF. This limitation was unavoidable in the experimental design because there was not enough space available on the optical bench to allow for the beam to be magnified to pass through the GAFs, then demagnified to continue down each path.

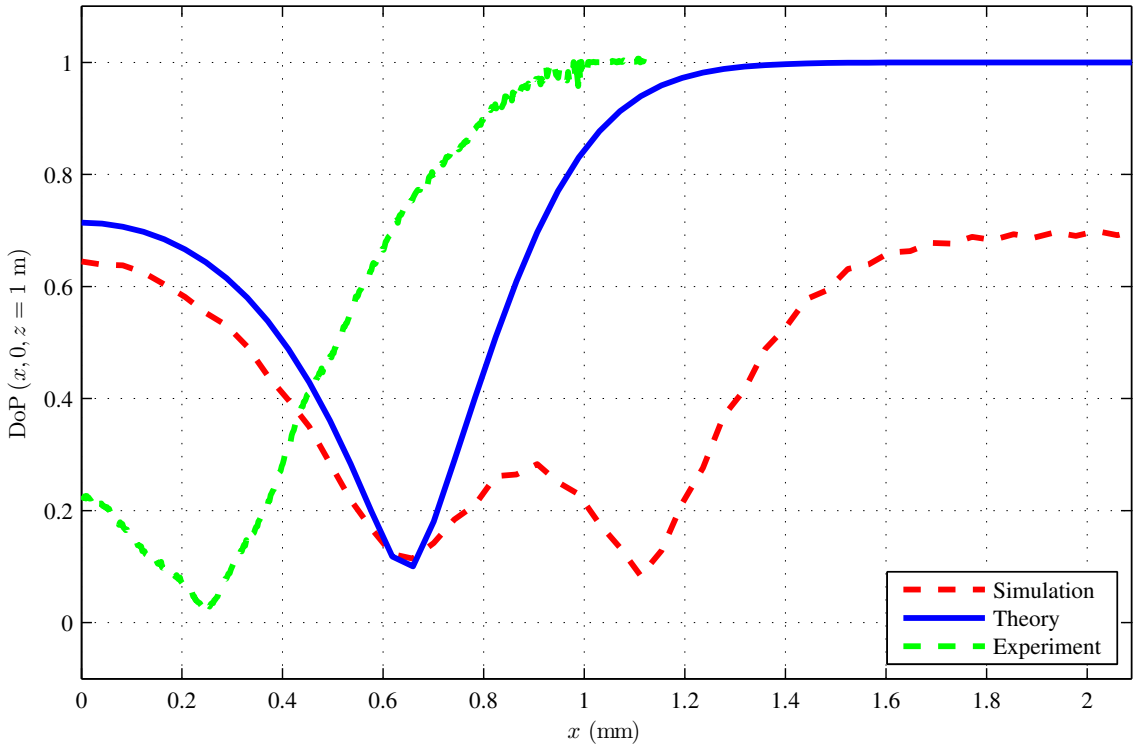

Figure 4.3: Experiment I degree of polarization results for theory, simulation, and experiment.

Figure 4.3 shows the DoP of the on-axis field with theoretical, simulation, and experimental results plotted together. The figure shows that, in general, the DoP of the field on axis changes on propagation and the experimental and theory approach unity. The simulation DoP does not approach unity due to the previously mentioned issue with the

GAF being too large for the SLM. The rate at which the experimental DoP changes does not match well with simulation or theory. This is most likely due to the experimental phase retardance being unknown yet still generating the CSDM cross-terms with a populated value for $|B_{xy}|$.

Figure 4.4 shows the experimental results for the irradiance correlation function compared to the results of simulation and theory. The images are organized such that the theoretical, simulation, and experimental results are along the columns—theoretical results are Figs. 4.4(a), 4.4(d), 4.4(g), and 4.4(j); simulation results are Figs. 4.4(b), 4.4(e), 4.4(h), and 4.4(k); experimental results are Figs. 4.4(c), 4.4(f), 4.4(i), and 4.4(l). Each row of images in Fig. 4.4 is a different irradiance correlation result—$\langle I_x(x_1, y_1)I_x(x_2, y_2)\rangle$ are Figs. 4.4(a), 4.4(b), and 4.4(c); $\langle I_x(x_1, y_1)I_y(x_2, y_2)\rangle$ are Figs. 4.4(d), 4.4(e), and 4.4(f); $\langle I_y(x_1, y_1)I_x(x_2, y_2)\rangle$ are Figs. 4.4(g), 4.4(h), and 4.4(i); $\langle I_y(x_1, y_1)I_y(x_2, y_2)\rangle$ are Figs. 4.4(j), 4.4(k), and 4.4(l). Figure 4.5 shows slices of the irradiance correlation functions for additional visualization of the results. The plots are organized such that the theoretical, simulation, and experimental curves overlay each other for each irradiance correlation result—$\langle I_x(x_1, y_1)I_x(x_2, y_2)\rangle$ is Fig. 4.5(a), $\langle I_x(x_1, y_1)I_y(x_2, y_2)\rangle$ is Fig. 4.5(b), $\langle I_y(x_1, y_1)I_x(x_2, y_2)\rangle$ is Fig. 4.5(c), and $\langle I_y(x_1, y_1)I_y(x_2, y_2)\rangle$ is Fig. 4.5(d).

The results in Figs. 4.4 and 4.5 showing the irradiance correlation functions $\langle I_\alpha(x_1, y_1)I_\beta(x_2, y_2)\rangle$ show very good agreement between the experimental, simulated, and theoretical data, thus validating the ability to control the coherence properties of the EGSM beam.

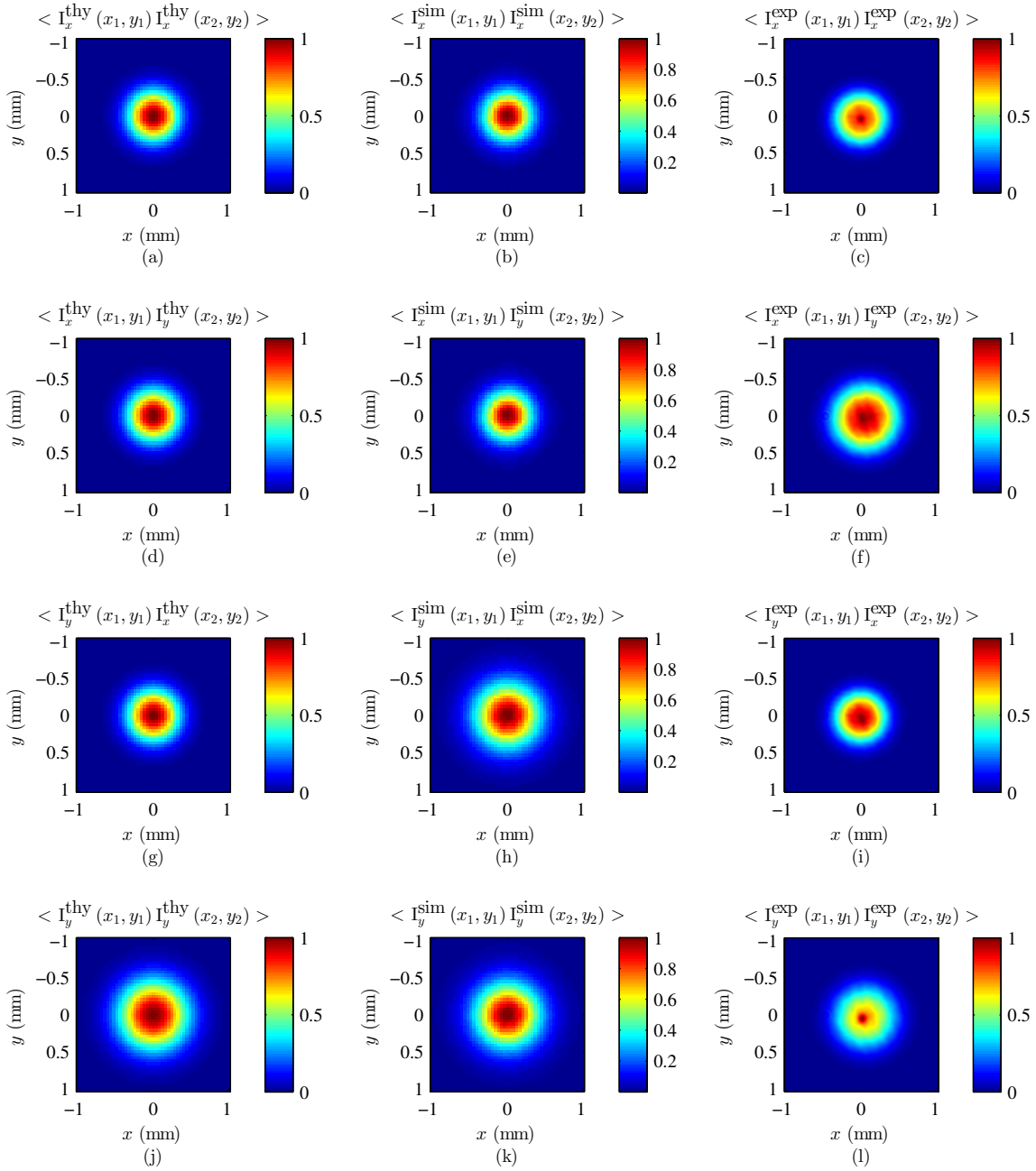

Figure 4.4: Experiment I irradiance correlation function results compared with simulation and theory. The rows are $\langle I_x(x_1, y_1) I_x(x_2, y_2) \rangle$, $\langle I_x(x_1, y_1) I_x(x_2, y_2) \rangle$, $\langle I_x(x_1, y_1) I_x(x_2, y_2) \rangle$, and $\langle I_x(x_1, y_1) I_x(x_2, y_2) \rangle$, respectively, while the columns are the theory, simulation, and experimental results, respectively.

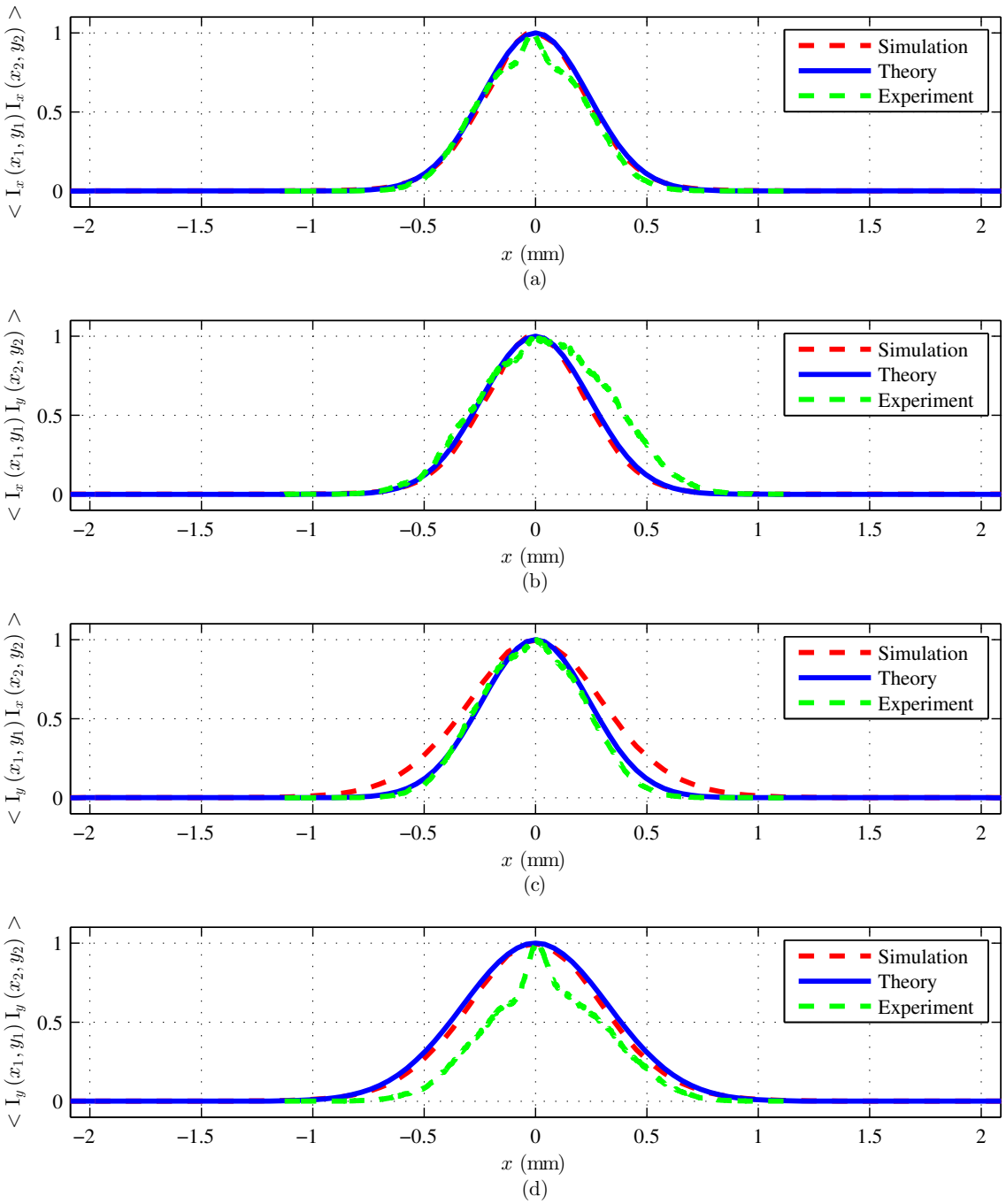

Figure 4.5: Experiment I irradiance correlation function results compared with simulation and theory. The theory, simulation, and experiment slices plotted together for each of (a) $\langle I_x(x_1, y_1) I_x(x_2, y_2)\rangle$, (b) $\langle I_x(x_1, y_1) I_y(x_2, y_2)\rangle$, (c) $\langle I_y(x_1, y_1) I_x(x_2, y_2)\rangle$, and (d) $\langle I_y(x_1, y_1) I_y(x_2, y_2)\rangle$.

4.2 Experiment II Results

Experiment II was completed using 1,000 realizations to generate the EGSM source. Figure 4.6 shows the experimental results for the Stokes parameters compared to the results of 1,000 simulations and theory. The images are organized such that the theoretical, simulation, and experimental results are along the columns—theoretical results are Figs. 4.6(a), 4.6(d), 4.6(g), and 4.6(j); simulation results are Figs. 4.6(b), 4.6(e), 4.6(h), and 4.6(k); experimental results are Figs. 4.6(c), 4.6(f), 4.6(i), and 4.6(l). Each row of images in Fig. 4.6 is a Stokes parameter—S_0 are Figs. 4.6(a), 4.6(b), and 4.6(c); S_1 are Figs. 4.6(d), 4.6(e), and 4.6(f); S_2 are Figs. 4.6(g), 4.6(h), and 4.6(i); S_3 are Figs. 4.6(j), 4.6(k), and 4.6(l). Figure 4.7 shows slices of the Stokes parameters for additional visualization of the results. The plots are organized such that the theoretical, simulation, and experimental curves overlay each other for each Stokes parameter—S_0 is Fig. 4.7(a), S_1 is Fig. 4.7(b), S_2 is Fig. 4.7(c), and S_3 is Fig. 4.7(d).

Overall the experimental Stokes parameters in Fig. 4.6 match the shape of the simulated and theoretical parameters well, showing good agreement. Noticeable for the experimental results for S_1 in Fig. 4.6(f) is the same apparent shift of the absolute value of the maxima at the center of the beam as in Experiment I. This is again due to spatial registration issues [20]. The results for S_2 and S_3 are negligible because the source parameters used have CSDM terms $W_{xy} = W_{yx} = 0$. Further, the simulation and theoretical results visible in Fig. 4.7 again do not match as well as published results [2]. This is due to the fact that the SLM is cropping the beam prior to passing through the GAF as described earlier.

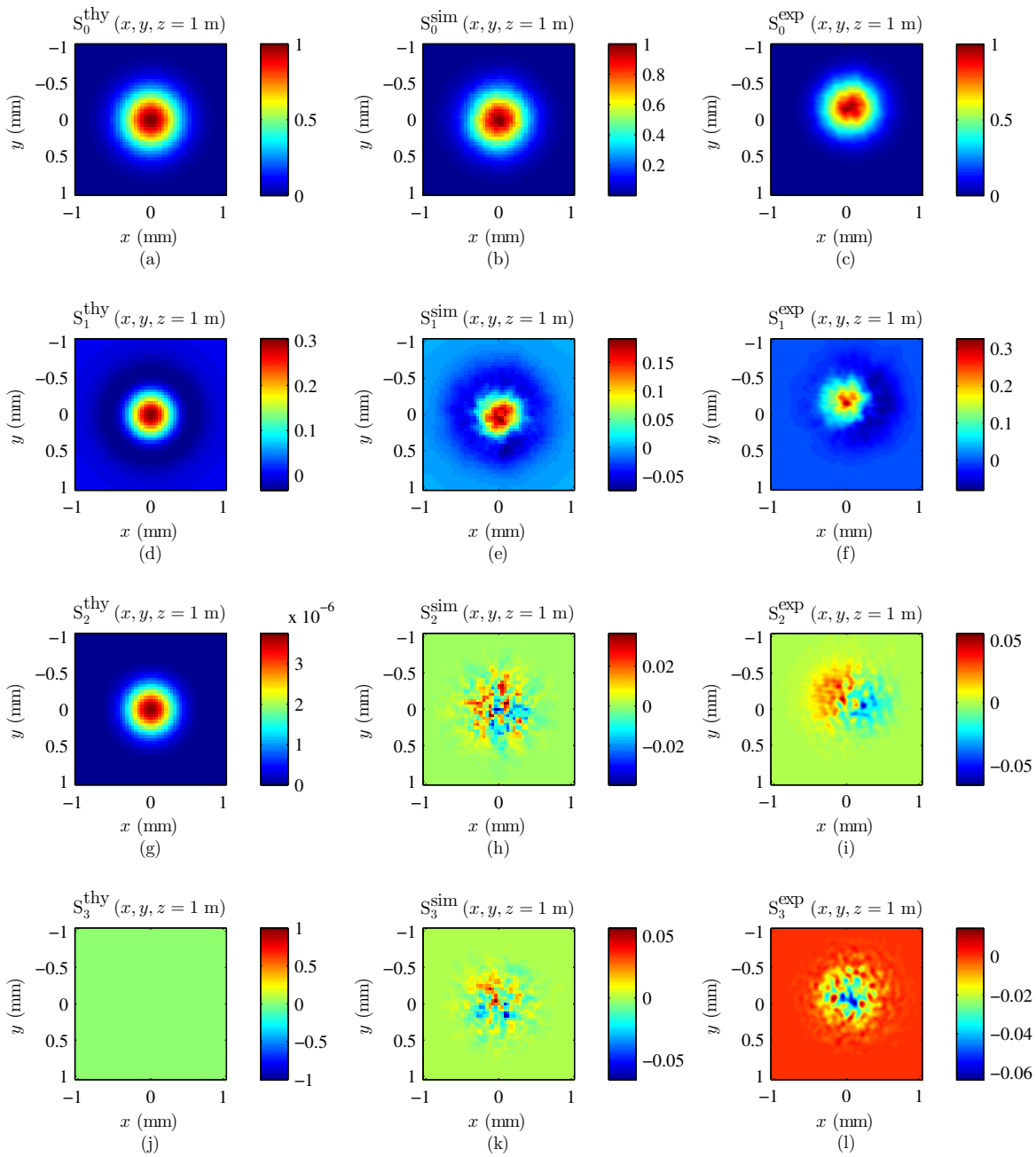

Figure 4.6: Experiment II Stokes parameter results compared with simulation and theory. The rows are S_0, S_1, S_2, and S_3, respectively, while the columns are the theory, simulation, and experimental results, respectively.

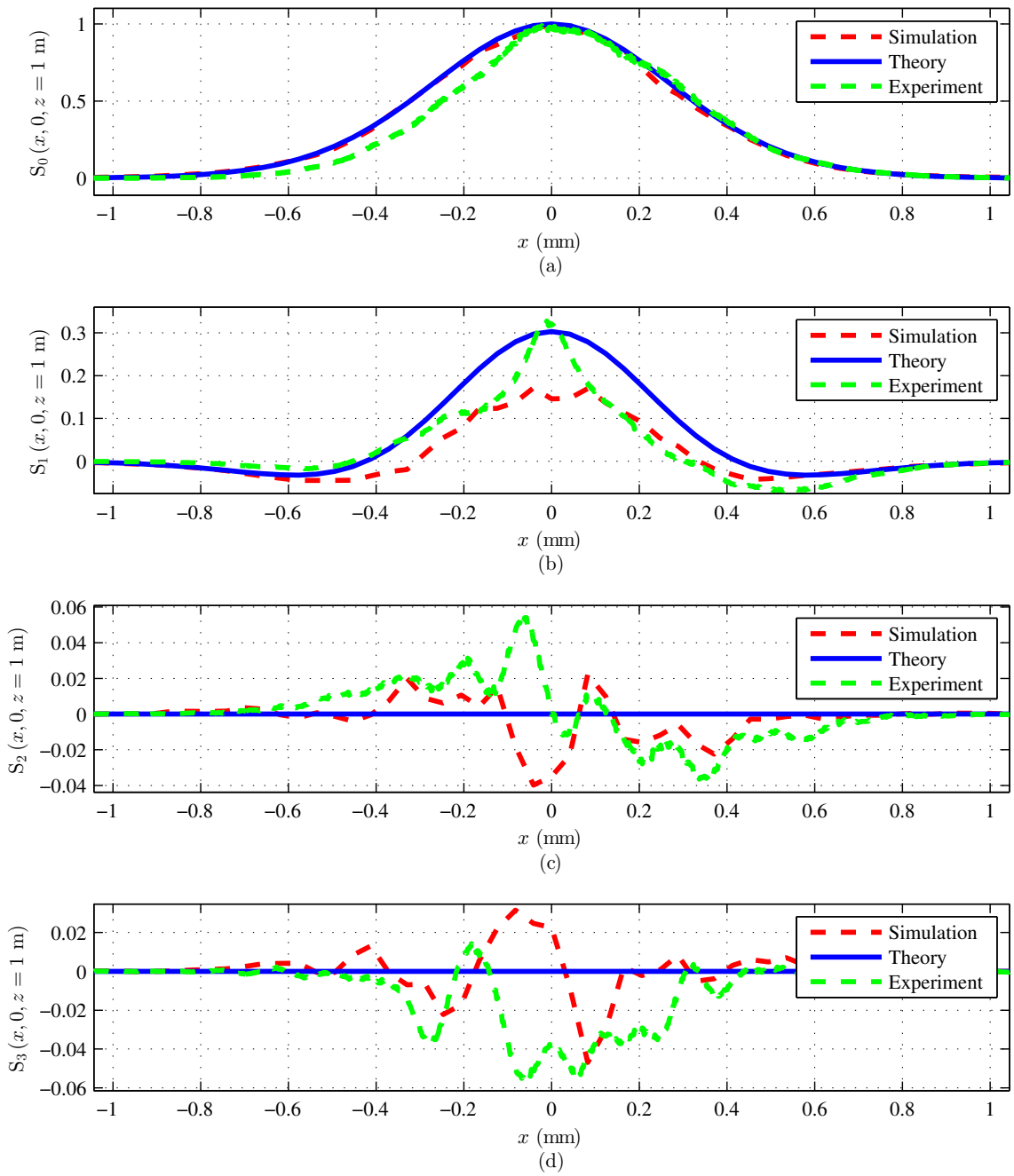

Figure 4.7: Experiment II Stokes parameter results compared with simulation and theory. The theory, simulation, and experiment slices plotted together for each of (a) S_0, (b) S_1, (c) S_2, and (d) S_3.

Figure 4.8 shows the DoP of the on-axis field with theoretical, simulation, and experimental results plotted together. The figure shows that, in general, the DoP of the field on axis changes on propagation and the experimental and theory approach unity. The simulation DoP does not approach unity again due to an issue with the GAF being too large for the SLM. The rate at which the DoP changes shows very good agreement between experimental, simulation, and theoretical results, thus validating the ability to control the polarization properties of the EGSM beam.

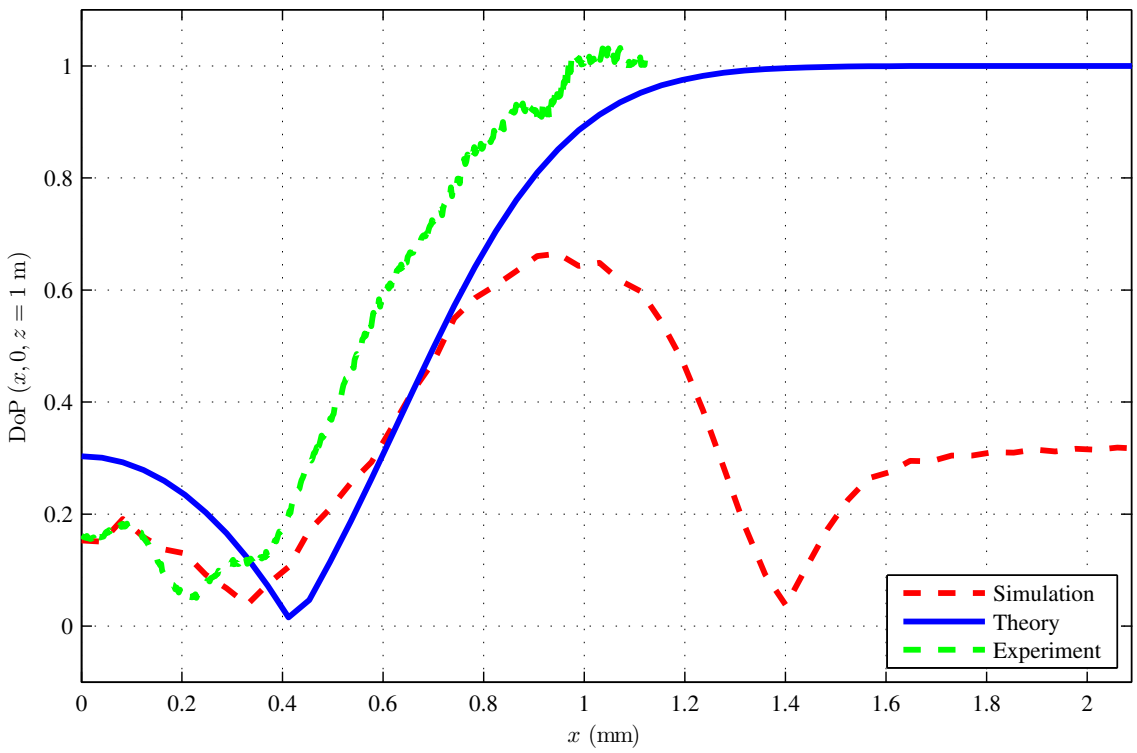

Figure 4.8: Experiment II degree of polarization results for theory, simulation, and experiment.

Figure 4.9 shows the experimental results for the irradiance correlation function compared to the results of simulation and theory. The images are organized such that

the theoretical, simulation, and experimental results are along the columns—theoretical results are Figs. 4.9(a), 4.9(d), 4.9(g), and 4.9(j); simulation results are Figs. 4.9(b), 4.9(e), 4.9(h), and 4.9(k); experimental results are Figs. 4.9(c), 4.9(f), 4.9(i), and 4.9(l). Each row of images in Fig. 4.9 is a different irradiance correlation result—$\langle I_x(x_1, y_1) I_x(x_2, y_2)\rangle$ are Figs. 4.9(a), 4.9(b), and 4.9(c); $\langle I_x(x_1, y_1) I_y(x_2, y_2)\rangle$ are Figs. 4.9(d), 4.9(e), and 4.9(f); $\langle I_y(x_1, y_1) I_x(x_2, y_2)\rangle$ are Figs. 4.9(g), 4.9(h), and 4.9(i); $\langle I_y(x_1, y_1) I_y(x_2, y_2)\rangle$ are Figs. 4.9(j), 4.9(k), and 4.9(l). Figure 4.10 shows slices of the irradiance correlation function for additional visualization of the results. The plots are organized such that the theoretical, simulation, and experimental curves overlay each other for each irradiance correlation result—$\langle I_x(x_1, y_1) I_x(x_2, y_2)\rangle$ is Fig. 4.10(a), $\langle I_x(x_1, y_1) I_y(x_2, y_2)\rangle$ is Fig. 4.10(b), $\langle I_y(x_1, y_1) I_x(x_2, y_2)\rangle$ is Fig. 4.10(c), and $\langle I_y(x_1, y_1) I_y(x_2, y_2)\rangle$ is Fig. 4.10(d).

The results in Figs. 4.9 and 4.10 showing the irradiance correlation functions $\langle I_\alpha(x_1, y_1) I_\beta(x_2, y_2)\rangle$ show very good agreement between the experimental, simulated, and theoretical data, thus further validating the ability to control the coherence properties of the EGSM beam.

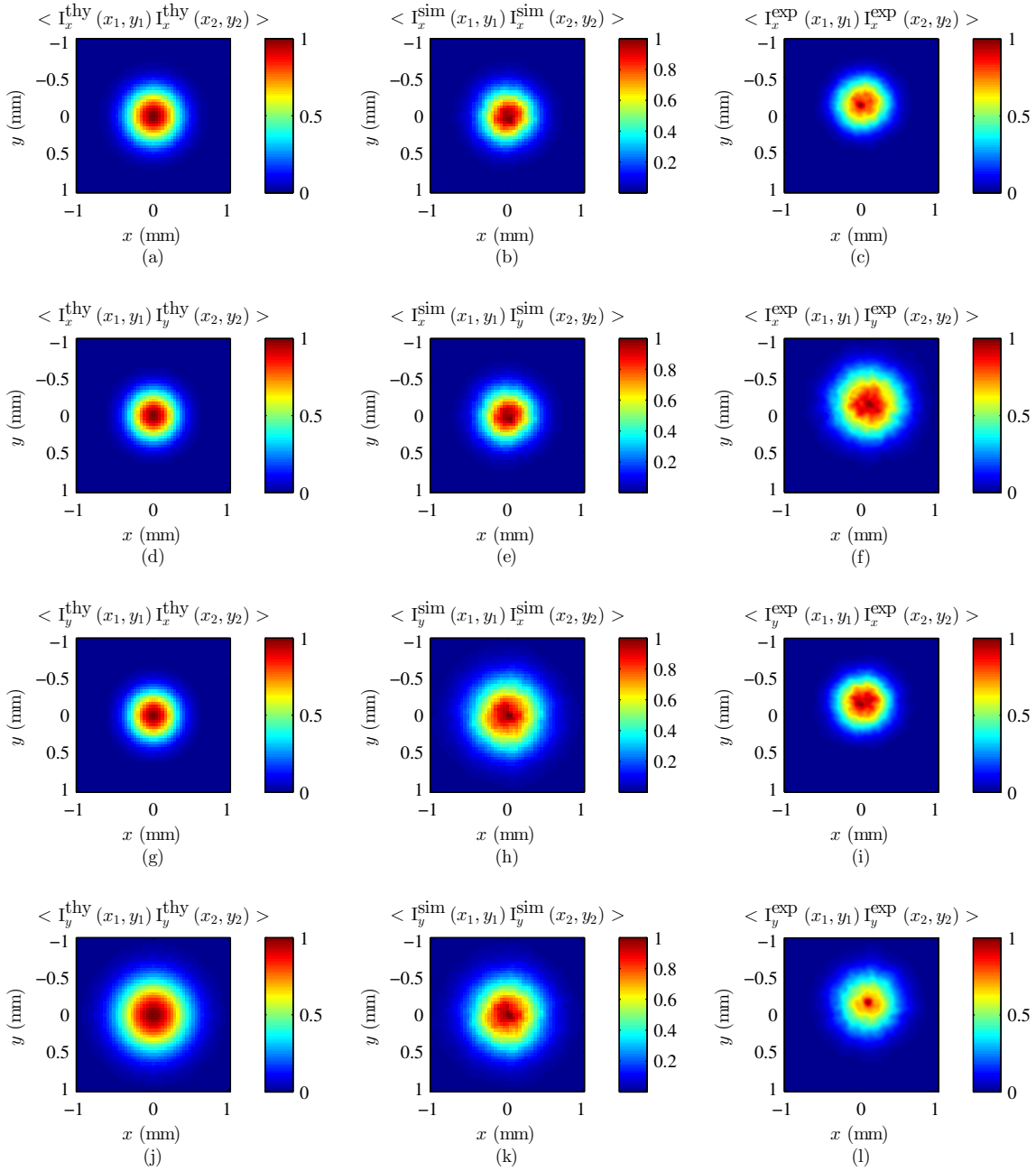

Figure 4.9: Experiment II irradiance correlation function results compared with simulation and theory. The rows are $\langle I_x(x_1, y_1) I_x(x_2, y_2) \rangle$, $\langle I_x(x_1, y_1) I_x(x_2, y_2) \rangle$, $\langle I_x(x_1, y_1) I_x(x_2, y_2) \rangle$, and $\langle I_x(x_1, y_1) I_x(x_2, y_2) \rangle$, respectively, while the columns are the theory, simulation, and experimental results, respectively.

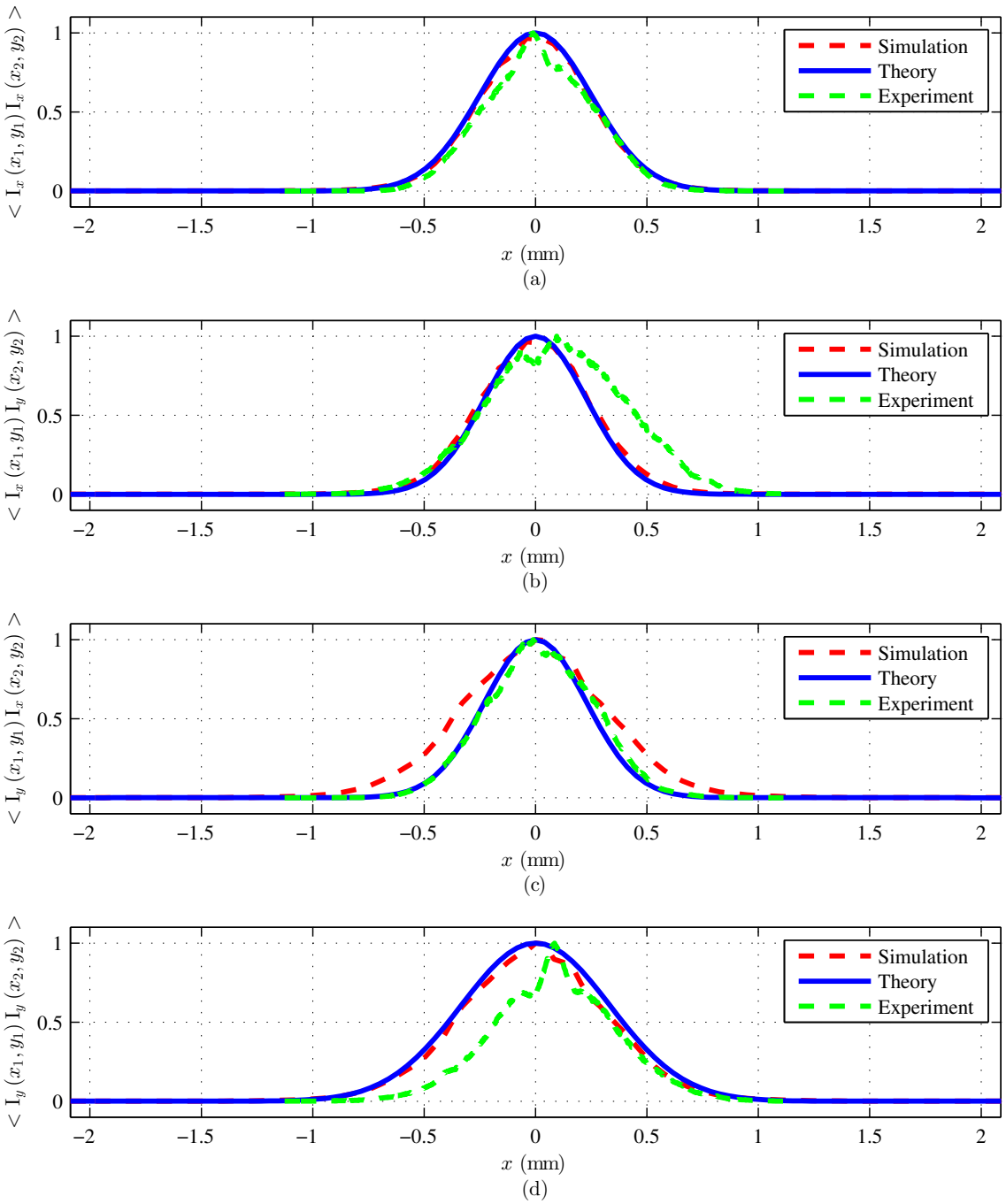

Figure 4.10: Experiment II irradiance correlation function results compared with simulation and theory. The theory, simulation, and experiment slices plotted together for each of (a) $\langle I_x(x_1, y_1) I_x(x_2, y_2)\rangle$, (b) $\langle I_x(x_1, y_1) I_y(x_2, y_2)\rangle$, (c) $\langle I_y(x_1, y_1) I_x(x_2, y_2)\rangle$, and (d) $\langle I_y(x_1, y_1) I_y(x_2, y_2)\rangle$.

V. Conclusions and Recommendations

5.1 Conclusions of Research

The experimental design demonstrated in this research has been shown to successfully produce EGSM beams. The generation of the beam was accomplished using two mutually orthogonal polarized components of initially coherent beams with Gaussian amplitudes which are phase modulated by a sequence of two mutually correlated random phase screens at the source plane. Coherence and polarization statistics were calculated on the integrated results and compared to published simulated and theoretical results to validate the experimental design [2, 17].

Although EGSM beams were successfully created, the accuracy of the results suffers without the calibration of all electro-optical components used in the beam generation and data capture. However, based on the results obtained in this research, the experimental design provides a viable method for generating EGSM beams with prescribed coherence and polarization properties. With the use of LC SLMs, exchangeable amplitude filters, and a LC VR, the design is highly configurable to generate EGSM beams with a wide range of properties for application in free-space optical communication, remote sensing, and directed energy.

5.2 Recommendations for Future Research

In this research, the experimental design was created and tested for viability. Future work would first entail a more thorough effort on calibration of the electro-optical devices used, i.e., the SLMs, the VR, and the detectors. This would both reduce error associated with aberrations and linear phase response, but also allow the ability to accurately measure all spectral Stokes parameters to provide more accurate results.

In addition to calibration, new SLMs and detectors could be used. The new SLMs could provide a higher resolution, greater pixel density, larger array size, 16-bit operation, and compatibility with 64-bit host operating systems to improve memory shortcomings. A division of amplitude polarimeter could be used as a new detector, allowing the simultaneous capture of three full resolution polarimetrically filtered images from which Stokes parameters can be computed [20]. This would eliminate the need for a rotatable polarization analyzer which may cause image registration errors.

With regard to the SLM, this device could be used for more than simply displaying the phase screens. There is potential for applying the amplitude filter and phase retardance on the SLM. Combining these elements on the SLM would eliminate the need for the GAFs, VR, and two of the four 4-f systems in the experimental design. The removal of these elements would reduce error associated with aberrations or misalignment. It would also provide a greater potential of producing non-Gaussian electromagnetic Schell-model (SM) beams or "designer beams."

Lastly, with regard to the physical design of the experiment, the 4-f lens systems could be configured to demagnify the SLM plane so the EGSM source plane could be captured by a detector rather than the EGSM observation plane. Additionally, the EGSM source plane could be simulated to propagate through the atmosphere using either an atmospheric phase wheel or using additional SLMs to display atmospheric phase screens. Further, the source plane could be reflected off an object to analyze the scattered light. Both of these proposals have a direct impact on experimentally verifying theory using EGSM beams for free-space optical communication and remote sensing.

Bibliography

[1] Avramov-Zamurovic, S., C. Nelson, R. Malek-Madani, and O. Korotkova. "Polarization-induced reduction in scintillation of optical beams propagating in simulated turbulent atmospheric channels". *Waves in Random and Complex Media*, 24:452–462, 2014. ISSN 1745-5030. http://www.tandfonline.com/doi/abs/10.1080/17455030.2014.944242.

[2] Basu, Santasri, Milo W. Hyde, Xifeng Xiao, David G. Voelz, and Olga Korotkova. "Computational approaches for generating electromagnetic Gaussian Schell-model sources". *Optics Express*, 22(26):31691, December 2014. ISSN 1094-4087. http://www.opticsinfobase.org/abstract.cfm?URI=oe-22-26-31691.

[3] Boulder Nonlinear Systems, Inc. "Spatial Light Modulators XY Series". http://www.meadowlark.com/store/data_sheet/Datasheet_XYseries_SLM.pdf.

[4] Cai, Yangjian, Yahong Chen, and Fei Wang. "Generation and propagation of partially coherent beams with nonconventional correlation functions: a review [invited]." *Journal of the Optical Society of America. A, Optics, image science, and vision*, 31(9):2083–96, September 2014. ISSN 1520-8532. http://www.opticsinfobase.org/viewmedia.cfm?uri=josaa-31-9-2083&seq=0&html=true.

[5] Edmund Optics. "EO 5012M " CMOS Monochrome USB Camera", 1992.

[6] Goodman, Joseph W. *Statistical Optics*. John Wiley & Sons, Inc., New York, 1985.

[7] Gori, F, M Santarsiero, G Piquero, R Borghi, A Mondello, and R Simon. "Partially polarized Gaussian Schell-model beams", 2000.

[8] Gori, Franco, Massimo Santarsiero, R. Borghi, and V. Ramírez-Sánchez. "Realizability condition for electromagnetic Schell-model sources." *Journal of the Optical Society of America. A, Optics, image science, and vision*, 25(5):1016–21, May 2008. ISSN 1084-7529. http://www.ncbi.nlm.nih.gov/pubmed/18451907.

[9] James, Daniel F. V. "Change of polarization of light beams on propagation in free space". *Journal of the Optical Society of America A*, 11(5):1641, May 1994. ISSN 1084-7529. http://josaa.osa.org/abstract.cfm?URI=josaa-11-5-1641.

[10] Jose, Franklin N. *ISOLATION OF SPECKLE FOR TARGET-IN-THE-LOOP COHERENT BEAM COMBINING*. Thesis, Air Force Institute of Technology, 2014.

[11] Korotkova, Olga. *Random Light Beams: Theory and Applications*. CRC Press, Boca Raton, 2014. ISBN 978-1-4398-1950-0.

[12] Meemon, Panomsak, Mohamed Salem, Kye-Sung Lee, Maryam Chopra, and Jannick P. Rolland. "Determination of the coherency matrix of a broadband stochastic electromagnetic light beam", 2008.

[13] Ostrovsky, Andrey S, Gabriel Martínez-Niconoff, Victor Arrizón, Patricia Martínez-Vara, Miguel a Olvera-Santamaría, and Carolina Rickenstorff-Parrao. "Modulation of coherence and polarization using liquid crystal spatial light modulators." *Optics express*, 17(7):5257–5264, 2009. ISSN 1094-4087.

[14] Ostrovsky, Andrey S., Gustavo Rodríguez-Zurita, Cruz Meneses-Fabián, Miguel A. Olvera-Santamaría, and Carolina Rickenstorff-Parrao. "Experimental generating the partially coherent and partially polarized electromagnetic source". *Optics* . . . , 18(12):12864–12871, 2010. http://www.opticsinfobase.org/abstract.cfm?uri=oe-18-12-12864.

[15] Piquero, G., F. Gori, P. Romanini, M. Santarsiero, R. Borghi, and A. Mondello. "Synthesis of partially polarized Gaussian Schell-model sources". *Optics Communications*, 208:9–16, 2002. ISSN 00304018.

[16] Roychowdhury, Hema and Olga Korotkova. "Realizability conditions for electromagnetic Gaussian Schell-model sources". *Optics Communications*, 249(4-6):379–385, 2005. ISSN 00304018.

[17] Sahin, Serkan, Zhisong Tong, and Olga Korotkova. "Sensing of semi-rough targets embedded in atmospheric turbulence by means of stochastic electromagnetic beams". *Optics Communications*, 283(22):4512–4518, November 2010. ISSN 00304018. http://linkinghub.elsevier.com/retrieve/pii/S0030401810004177http://www.sciencedirect.com/science/article/pii/S0030401810004177.

[18] Salem, Mohamed and Olga Korotkova. "Polarization changes in partially coherent electromagnetic beams propagating through turbulent atmosphere". *Waves in Random* . . . , 14(4):513–523, October 2004. ISSN 0959-7174. http://www.tandfonline.com/doi/abs/10.1088/0959-7174/14/4/003http://www.tandfonline.com/doi/pdf/10.1088/0959-7174/14/4/003.

[19] Schmidt, Jason D. *Free-space optical communications performance enhancement by use of single adaptive optics correcting element*. Dissertation, University of Dayton, 2006.

[20] Schott, John R. *Fundamentals of polarimetric remote sensing*. SPIE tutorial texts. SPIE, Bellingham, 2009. ISBN 9780819478764. http://encore.lib.gla.ac.uk/iii/encore/record/C__Rb2831838__S(Fresnel)(Reflect*)__P0,5__Orightresult__X1?lang=eng&suite=cobalt$\delimiter"026E30F$nhttp://encore.lib.gla.ac.uk/iii/encore/record/C__Rb2831838__S(polarimetr*)__P0,5__Orightresult__X2?lang=eng&suite=cobalt.

[21] Shirai, Tomohiro, Olga Korotkova, and Emil Wolf. "A method of generating electromagnetic Gaussian Schell-model beams". *Journal of Optics A: Pure and* . . . , 7(5):232–237, May 2005. ISSN 1464-4258. http://stacks.iop.org/1464-4258/7/i=5/a=004?key=crossref.ab847580988f01ec031cadafb9efffd0http://iopscience.iop.org/1464-4258/7/5/004.

[22] ThorLabs. "LCC1223-A - Full-Wave Liquid Crystal Retarder", 2012. http://www.thorlabs.com/thorproduct.cfm?partnumber=LCC1223-A.

[23] Wang, Fei, Gaofeng Wu, Xianlong Liu, Shijun Zhu, and Yangjian Cai. "Experimental measurement of the beam parameters of an electromagnetic Gaussian Schell-model source." *Optics letters*, 36(14):2722–4, July 2011. ISSN 1539-4794. http://ol.osa.org/abstract.cfm?URI=ol-36-14-2722.

[24] Wolf, Emil. "Unified theory of coherence and polarization of random electromagnetic beams". *Physics Letters A*, 312(5-6):263–267, June 2003. ISSN 03759601. http://linkinghub.elsevier.com/retrieve/pii/S0375960103006844http://www.sciencedirect.com/science/article/pii/S0375960103006844.

[25] Wolf, Emil. *Introduction to the Theory of Coherence and Polarizatoin of Light*. Cambridge University Press, New York, 2007.

[26] Xiao, Xifeng and David Voelz. "Wave optics simulation of partially coherent and partially polarized beam propagation in turbulence". *SPIE Optical Engineering+* . . . , 7464:74640T–74640T–11, August 2009. http://proceedings.spiedigitallibrary.org/proceeding.aspx?articleid=788082.

REPORT DOCUMENTATION PAGE

Form Approved
OMB No. 0704–0188

The public reporting burden for this collection of information is estimated to average 1 hour per response, including the time for reviewing instructions, searching existing data sources, gathering and maintaining the data needed, and completing and reviewing the collection of information. Send comments regarding this burden estimate or any other aspect of this collection of information, including suggestions for reducing this burden to Department of Defense, Washington Headquarters Services, Directorate for Information Operations and Reports (0704–0188), 1215 Jefferson Davis Highway, Suite 1204, Arlington, VA 22202–4302. Respondents should be aware that notwithstanding any other provision of law, no person shall be subject to any penalty for failing to comply with a collection of information if it does not display a currently valid OMB control number. **PLEASE DO NOT RETURN YOUR FORM TO THE ABOVE ADDRESS.**

1. REPORT DATE *(DD–MM–YYYY)*	2. REPORT TYPE	3. DATES COVERED *(From — To)*
26–03–2015	Master's Thesis	Oct 2014–Mar 2015

4. TITLE AND SUBTITLE

Experimental method of generating electromagnetic Gaussian Schell-model beams

5a. CONTRACT NUMBER

5b. GRANT NUMBER

F4FGA04013J001

5c. PROGRAM ELEMENT NUMBER

6. AUTHOR(S)

Gridley, Matthew J., Captain, USAF

5d. PROJECT NUMBER

ENGJON451A

5e. TASK NUMBER

5f. WORK UNIT NUMBER

7. PERFORMING ORGANIZATION NAME(S) AND ADDRESS(ES)

Air Force Institute of Technology
Graduate School of Engineering and Management (AFIT/EN)
2950 Hobson Way
WPAFB, OH 45433-7765

8. PERFORMING ORGANIZATION REPORT NUMBER

AFIT-ENG-MS-15-M-058

9. SPONSORING / MONITORING AGENCY NAME(S) AND ADDRESS(ES)

Air Force Office of Scientific Research, Julie Moses, PhD
3875 Randolph St., Suite 348
Arlington, VA 22203
(703) 696-9586, julie.moses@us.af.mil

10. SPONSOR/MONITOR'S ACRONYM(S)

AFOSR/RTB

11. SPONSOR/MONITOR'S REPORT NUMBER(S)

12. DISTRIBUTION / AVAILABILITY STATEMENT

DISTRIBUTION STATEMENT A:
APPROVED FOR PUBLIC RELEASE; DISTRIBUTION UNLIMITED

13. SUPPLEMENTARY NOTES

This work is declared a work of the U.S. Government and is not subject to copyright protection in the United States.

14. ABSTRACT

The purpose of this research effort is to experimentally generate an electromagnetic Gaussian Schell-model beam from two coherent linearly polarized plane waves. The approach uses a sequence of mutually correlated random phase screens on phase-only liquid crystal spatial light modulators at the source plane. The phase screens are generated using a published relationship between the screen parameters and the desired electromagnetic Gaussian Schell-model source parameters. The approach is verified by comparing the experimental results with published theory and numerical simulation results. This work enables the design of an electromagnetic Gaussian Schell-model source with prescribed coherence and polarization properties.

15. SUBJECT TERMS

electromagnetic Gaussian Schell-model, EGSM, GSM, partially coherent, partially polarized

16. SECURITY CLASSIFICATION OF:			17. LIMITATION OF ABSTRACT	18. NUMBER OF PAGES	19a. NAME OF RESPONSIBLE PERSON
a. REPORT	b. ABSTRACT	c. THIS PAGE			Maj Milo W. Hyde IV, PhD (ENG)
U	U	U	UU	73	19b. TELEPHONE NUMBER *(include area code)* (937) 255-3636 x4371 Milo.Hyde@afit.edu

Standard Form 298 (Rev. 8–98)
Prescribed by ANSI Std. Z39.18